Journal of Mining and Environment (JME) Vol. 15, No. 3, 2024, 791-816

Shahrood University of Technology

Journal of Mining and Environment (JME)

Journal homepage: www.jme.shahroodut.ac.ir

Iranian Society of Mining Engineering (IRSME)

Mineral Prospectivity Modeling over Julie Tenement of Northwestern Ghana using Geophysical Datasets

Prince Ofori Amponsah[1], and Eric Dominic Forson[2*]

1. Department of Earth Science, School of Physical and Mathematical Science, University of Ghana, Legon-Accra, Ghana
2. Department of Physics, School of Physical and Mathematical Sciences, University of Ghana, Legon-Accra, Ghana

Article Info

Received 20 September 2023
Received in Revised form 11 October 2023
Accepted 3 January 2023
Published online 3 January 2023

DOI: 10.22044/jme.2024.13636.2519

Keywords

Mineral prospectivity modeling
Information value
Weight of evidence
Aeromagnetic data
Airborne radiometric data

Abstract

This study was set out to delineate prospective zones of gold mineralization occurrence over the Julie tenement of Northwestern Ghana using two spatial statistical techniques, namely information value (IV) and weight of evidence (W of E) models. First, 110 locations, where gold (Au) mineralization has been observed, were identified by field survey results derived from highly anomalous geo-chemical assay datasets. Of these 110 locations, 77 (representing 70% of the known locations, where gold has been observed) were randomly selected for training the aforementioned models, and the remaining 33 (analogous to 30% of the known Au occurrence) were used for validation. Secondly, eleven mineral conditioning factors (evidential layers) comprising analytic signal, reduction-to-equator (RTE), lineament density (LD), porphyry density, potassium concentration, thorium concentration, uranium concentration, potassium-thorium ratio, uranium-thorium ratio, geology, and arsenic concentration layers were sourced from geo-physical, geological, and geo-chemical datasets. Subsequently, by synthesizing these eleven evidential layers using the two spatial statistical techniques, two mineral prospectivity models were created in a geographic information system (GIS) environment. Finally, the mineral prospectivity models produced were validated using the area under the receiver operating characteristics curve (AUC). The results obtained showed that the IV model produced had a higher prediction accuracy in comparison with the mineral predictive model produced by the W of E with their AUC scores being 0.751 and 0.743, respectively.

1. Introduction

Access to mineral resources through mineral exploration and exploitation over the years has brought immeasurable economic benefits to many wealthy nations (Australia, Canada, USA, South Africa, and the like) around the world, and has the potential to enrich many more transitional and developing economies [1,2,3]. The potential wealth seen by many of these developing nations has driven them to find innovative ways in the discovery of these mineral resources, which Ghana is no exception. Despite Ghana's impressive continual economic growth mainly underpinned by the exportation of its mineral resources (mainly from gold), the country still faces budget deficits and rising debt to gross domestic product (GDP) ratios. This means that the country will have to find more of these resources in order to boost its foreign currency reserves and correct its budget deficits. Thus, there is a need to delineate newly prospective zones of mineral occurrences, which will have a ripple effect on the economic fortunes of the country (Ghana). The first step in carrying out a mineral prospectivity model over an area of interest is the acquisition of geo-spatially characterized geoscientific datasets. For this reason, Azumah Resources Limited carried out a multi-disciplinary exploration scheme, which encompassed geological and structural mapping; soil, rock, and auger point sampling; diamond drilling to define bedrock mineralization; as well as high-resolution geo-physical data acquisition encompassing magnetic and radiometric [4]The

Corresponding author: edforson@ug.edu.gh (E. Dominic Forson)

second step that is critical to mineral prospectivity modeling (MPM) concerns the selection of the appropriate geo-scientific criteria that are essential for the characterization of the sought-after mineral deposit. The third most important step in MPM is the generation of evidential layers from the geo-spatial dataset based on the appropriate geo-scientific criteria selected. The final stage in MPM is essentially hinged on synthesizing the generated evidential layers towards the end goal of producing a predictive model that outlines the mineral prospects or target zones of essential mineral resources [5,6,7].

In synthesizing various evidential layers towards the generation of a mineral prospectivity model, the use of geographic information systems and multi-source data integration techniques have been employed. These techniques generally come in two models, knowledge-driven models and data-driven models. In carrying out knowledge-driven models, the weight of the evidential layers derived are assigned by incorporating opinions of mineral exploration geo-scientists [4,6,8]. In the generation of mineral prospectivity models in a data-driven way, the influence (weight) of the chosen evidential layers towards the production of the model is dependent on their spatial relationship to existing data of the mineral occurrence. Mineral predictive modeling can also be carried out in a hybrid manner by incorporating both known locations of mineral occurrences and expert opinions of mineral exploration geoscientists. Thus the use of knowledge-driven models [3,9,10,11,12], data-driven models [13,14,15,16,17,18], and a blend of the aforementioned two main models [7,19, 20,21]20 have been found applicable in delineating prospectively viable zones of mineral occurrence in various geologic environments. It is important to note that the use of data-driven methods for predictive modeling is preferable when employed in regions with significant amount of known mineral occurrences. This is because data-driven methods are viable for assessing the relationship between known locations of mineral occurrences and various classes of selected evidential layers [15]. They are deemed to produce models with improved accuracy. In this study, the Julie Tenement was chosen as a case study for a data-driven based mineral predictive modeling using the weight of evidence (WofE) and information value (IV) techniques because it is currently the tenement with the largest mineral prospects within the northwestern part of Ghana [22]. It is, therefore, important to note that there is no systematically generated model that outlines the mineral potential over the tenement despite the availability of geoscientific datasets (such as magnetic and radiometric datasets) as well as the delineated known locations of mineral occurrences to facilitate such course. Thus, the creation of an effective mineral prospectivity map would be required in order to intuitively harness various exploration programs in the tenement in the future. In view of this, this study seeks to carry out a comparative performance assessment of mineral prospectivity models that would be generated based on the Wof E and IV techniques over the Julie tenement of Ghana's northwestern part. Since models generated are irrelevant until they have been duly validated [23], the receiver operating characteristic curve would be employed to assess the performance of the MPM to be generated in this study. It is conceived that the MPM outputs generated in this study would have guide various mineral exploration programs within the Julie tenement and other areas in the northwestern part of Ghana.

2. Studied area and geological setting

2.1. Studied area

The Julie tenement (marked as white in Figure 1) is located in the Upper West Region of Ghana (thus NW Ghana) specifically the Wa-East district and lies within the longitude 2°10'13" E to 2°12'44" E and latitude 10°05'14" N to 10°09'15" N based on the WGS datum ellipsoid. The topography in the studied area is generally flat due to the extensive erosion the area has experienced, with topographic height ranging from 290 m to 400 m. The only river that drains the tenement is the Felin River. The studied area according to Dickson and Benneh [24] is characterized by the Guinea Savannah vegetation typified by grasses of different heights and interspersed with fire-resistant deciduous trees.

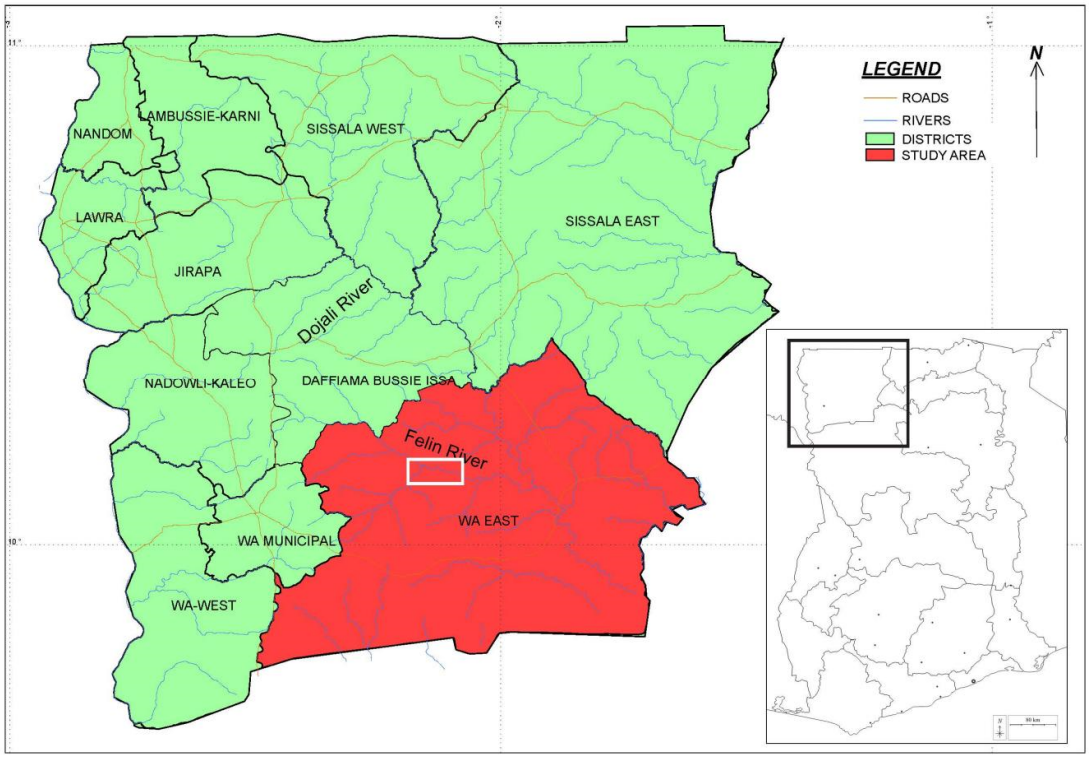

Figure 1. Map of the northwestern Ghana showing various administrative districts (studied area is marked in white).

2.2. Geological setting

The geology of NW Ghana lies within the 2250-1980 Ma Eburnean tectono-magmatic Birimian terrane (Figure 2(a)), which is responsible for the formation of greenstone belts and associated granitoids [25,26, 27]. The Birimian terrane in NW Ghana marks the eastern edge of the West African Craton, and is defined by the Julie greenstone belt, the Wa-Lawra belt, the Tumu-Koudougou terrane, and the Bole-Bulenga domain (Figure 2(b); [28]) The Julie tenement lies within the Julie greenstone belt [29], and is bounded to the west by the Wa-Lawra belt, to the north by the Tumu-Koudougou terrane, to the south by the Bole-Bulenga domain, and the east by the Bole-Nangondi belt. The north-south (N-S) oriented Wa-Lawra belt is divided into an eastern and western half by a 100 km north (N) to NNW (north-northwestern) oriented crustal scale transcurrent shear zone with sinistral characteristics known as the Jirapa shear zone or fault. The eastern part is composed of 2139 ± 2 Ma (detrital age of zircons; [30]) meta-greywackes, meta-volcanosediments, metashales (pelites; [30, 31,32,33]), and early syn-tectonic 2212 ± 1 Ma and 2153 ± 4 Ma granitoids [30,33]. These rocks have been intruded by late kinematic granitoids of 2104 ± 1 Ma [30,34,35]. The western half is composed of 2187 ± 3 Ma high grade para- and ortho-gneisses, rhyolites and granitoids [30] also connoting amphibolite to migmatite facies [28].

Juxtaposing the Wa-Lawra Belt eastwards by the Jang shear zone or fault is the Tumu-Koudougou terrane. This terrane is mainly defined by granitic complexes composed of 2162 ± 1 Ma to 2134 ± 1 Ma gneisses and gabbros. Intruding these rocks is the 2128 Ma porphyritic granites [30,31,32,33]. The Bole-Bulenga domain is composed of high-grade metamorphic rocks such as metabasites and paragneisses with migmatitic characteristics. These rocks have been termed as the Buki gneisses by De Kock et al. [36], and have been intruded by 2195 Ma and 2135 Ma granitoids [28,30]. In keeping with the structural interpretation (framework) made by various works in NW Ghana [28,34,37], the terrane has experienced a polycyclic structural event. The first deformation phase, D1 in NW Ghana is defined by N-S shortening crustal thickening event, marked by nappe stacking event. The second deformational event (D2) is marked by the N-S extension, which is characterized by extensional shear zones along the E-W margin of the Bole-Bulenga domain. D3 is marked by E-W or NE-SW shortening, which is responsible for the N-S or NNE-SSW. D4 is

characterized by WNW to ESE compression, whiles that of D5 is characterized by the dextral NE crustal scale strike slip shear zone. D6 in NW Ghana is marked by Pan-African E-W shorting and responsible for all the late N-S brittle faults.

2.3. Overview of mineralization and alteration style and controls on Julie tenement

The mineralization style associated with the Paleoproterozoic quartz lode gold in the Julie tenement is mainly based on the work done by Amponsah et al. [35] and *Amponsah* et al. [37] on the Julie deposit and the geological mapping done on the tenement by the authors. According to the space-time correlation done by Block et al. [28] in NW Ghana, the gold mineralization in the Julie tenement can be constrained to have occurred between 2145 and 2125 Ma. Like all orogenic gold deposits around the world, the temporal and spatial distribution of the gold mineralization on the tenement is associated with quartz veins in a deformed metamorphosed Julie greenstone belt or terrane with accretional or collisional characteristics [28]. The host rocks for the gold mineralization on the tenement are the metamorphosed greenschist facies granitoids with tonalitic affinities [35] and accreted oceanic metasedimentary sequences with subordinate volcanics interbedded with metapelites and volcaniclastics [4].

Tectonically, the gold mineralization on the tenement is associated with the brittle-ductile transition, second-order shear zones with dilation jogs and fault bifurcations, which are splays of the first-order E-W Baayiri fault [28,35]. In the granitoids, the gold mineralization manifests itself as a series of quartz veins or lodes in several sets (with varying lengths, mainly between 3 and 7 km) of shear zones formed from second-order low angle thrust with reverse characteristics. The higher degree of misorientation due to the reverse characteristics with respect to the E-W strike of the shear zones (thus the fault planes of the low angle thrust) in the granitoids generated a higher level of fluid over-pressure, making it susceptible to high fluid flux [37]. In the metasediments, the gold mineralization is associated with boudinage to transposed quartz veins within a moderate to steeply dipping (usually between 60 to 70 degrees) shear zone with an E-W strike and dip direction to the north. The gold mineralization in the tenement has a direct relationship with the structural traps. By way of orebody controls and geometry, the 20 m to 50 m thick quartz vein lodes are primarily within a series of 3 to 7 km shear zones associated with the granitoids and sediments in the Julie tenement.

The alteration mineral assemblages defining the 50 m bleached mineralized envelope within the granitoids consist of sericite + quartz + ankerite + k-feldspar + calcite ± tourmaline + pyrite and in the sediments, the mineralization envelop is defined by chlorite + ankerite + arsenopyrite ± pyrite ± graphite [35,37].

3. Methodology

3.1. Dataset

The geospatial datasets used for delineating mineral prospective zones with the Julie Tenement comprises geophysical, geological, and geochemical data. The geological data (which has a scale of 1:100,000), which was compiled by the Ghana Geological Survey Authority (GGSA) [30] was acquired to be employed in this study. The geo-chemical data used for this study was collected by Azumah Resources Limited (ARL) at a scale of 1:5000. The geo-physical datasets used for this study, which includes radiometric and magnetic data were acquired from ARL with a spatial resolution of 7.5 m [4]. In total, eleven evidential layers were extracted from the geo-physical, geological, and geo-chemical datasets. From the geo-physical datasets, the authors extracted nine evidential layers comprising analytic signal, lineament density, porphyry density, reduction-to-equator (from the magnetic data), thorium concentration, uranium concentration, potassium concentration, potassium-thorium ratio, and uranium-thorium ratio (from radiometric data) were derived. Asymmetric problems are common or prevalent for magnetic data acquired at low magnetic latitudes, for which the Julie tenement is an example. Thus, total magnetic intensity responses acquired and for that matter the total magnetic intensity grid obtained were reduced to equator (RTE), so that the magnetic signals observed are characteristic of sub-surface geological responses. In view of this, the RTE grid was generated. The analytic signal grid, which captures the spatial distribution of magnetic intensity gradient was also generated by applying the analytic signal filtering technique on the total magnetic intensities.

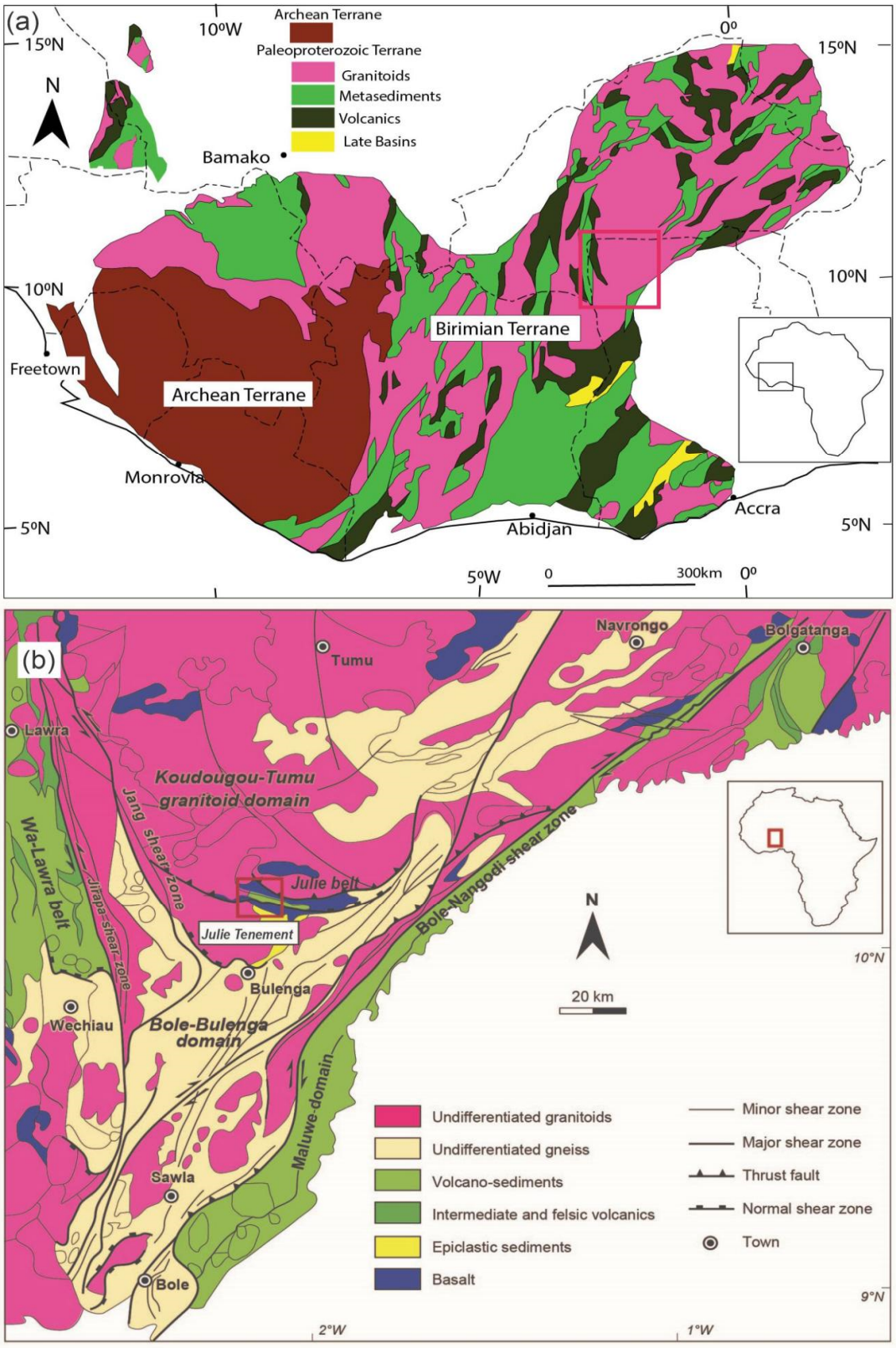

Figure 2. (a) Simplified geological map of the southern portion of the West African craton (modified after Milési et al. [38]) with the studied area indicated with a red box. The pink color indicates granitoids, with the light and deep green indicating volcanosedimentary and basaltic rock, respectively, whiles the yellow indicate the Tarkwaian sediments (b) simplified geological map of NW Ghana (modified after Block et al. [28]).

The individual radiometric channels comprising potassium (K), thorium (eTh), and uranium (eU) were each gridded using the Kriging method. Subsequently, the radiometric ratio grids comprising K/eTh and eU/eTh were also generated. The lineament density (LD) grid was produced based on the Center for Exploration Targeting (CET) grid analysis technique [39, 40]. The CET porphyry detection technique [41] was employed to delineate porphyry magnetic features (otherwise known as porphyry density) that may be associated with gold mineralization within the study area. Both the lineament density and the porphyry density layers were generated by employing their respective aforementioned techniques on the reduced-to-equator grid. All these grids were further imported in a GIS (geographic information system) environment in raster format. It is noteworthy that, the processing of the generation of the RTE, analytic signal, K, eTh, eU, K/eTh, eU/eTh, LD, and porphyry density grids were generated using the Geosoft Oasis Montaj software. In the case of the geochemical dataset, the arsenic concentration layer was generated by applying the inverse distance weighted (IDW) interpolation method on a point shapefile of arsenic values in parts-per-million (ppm) using ArcGIS 10.8. The geological layer though originally sourced in vector format was converted to raster format to conform with the other layers. In order to assess the spatial association of various classes within evidential layers and the existing locations of mineral occurrence based on the data-driven statistical techniques employed in this study, all these evidential layers were rescaled to have the same cell size of 3.03 m. This in effect produced a cell size of 3.03 m × 3.03 m, and thus the studied area was observed to be characterized by a total pixel count of 6708561. In order to efficiently apply the modeling techniques (comprising the weight of evidence and the information value) to determine the influence of each evidential layer towards the model to be generated, the natural breaking classification technique was employed in discretizing each of these evidential layers. A detailed description of why these evidential layers were identified and chosen for this study has been carried out in Section 4.1.

In carrying out predictive modeling in a data-driven way, the availability of a considerable number of existing locations of sought-after mineral occurrence is very critical towards the generation of the model. Thus 110 known gold (Au) locations, obtained from highly anomalous Au geo-chemical assay results and existing locations of artisanal mining operations (referred to as Au labels) within the tenement were used. These Au labels were apportioned randomly into two, to characterize training Au labels (made up of 70% of total Au labels) and the testing Au labels (comprising 30% of the total Au labels). To make the Au labels (which are point data in the form of X and Y coordinates) conscionably analogous and representative of the extent of the mineral to be explored in terms of scale, the Au labels were converted to pixels with a cell size of 3.03 m × 3.03 m [42,43]. In this regard, the transformation of the Au labels into the pixel format based on the aforementioned cell size resulted in the generation of a total Au occurrences pixel count of 1009 (with 706 as training pixels and 303 as a test or validation pixels) within the Julie Tenement.

3.2. Data-driven statistical methods

3.2.1. Weight of Evidence (WofE)

In mineral prospectivity modeling, the weight of evidence technique, which is a data-driven method was first used by Bonham-Carter [44] to evaluate mineral resources hypothetically based on a number of binary evidential layers denoted by BEV_1, BEV_2, BEV_3, $\cdots$ BEV_n. In WofE, a value of 0 is assigned to depict the unavailability of a feature; a value of 1 is also assigned to characterise the presence or availability of a particular feature. For an evaluation model, if the areal extent is divided into a grid of Z_G pixels, with the areal extent of the grids with known Au occurrences within the evidential layer being Au_G pixels, the prior probability $P(Au_G)$ can be estimated as shown in Equation 1.

$$P(Au_G) = \frac{Au_G}{Z_G} \quad (1)$$

The prior probability in Equation 1, can be expressed in terms of its corresponding odds ratio formula shown in Equation 2.

$$O(Au_G) = \frac{P(Au_G)}{1 - P(Au_G)} \quad (2)$$

Thus, for an evidential layer BEV_i, the weight of evidence can be computed as shown in Equations 3 and 4.

$$W_i^+ = \ln\left(\frac{P(BEV_i/Au_G)}{P(BEV_i/\overline{Au_G})}\right) \quad (3)$$

$$W_i^- = \ln\left(\frac{P(\overline{BEV_i}/Au_G)}{P(\overline{BEV_i}/\overline{Au_G})}\right) \quad (4)$$

W^+_I and W^-_I in Equations 3 and 4 denote the

weight of evidence for an ith class of an evidential layer when Au occurrences are respectively absent. $\overline{Au_G}$ represents the absence of Au occurrence, whereas Au_G denotes the presence of Au occurrence. $\overline{BEV_i}$ characterizes the absence of the ith class binary layer. Also, the posterior probability odds ($O_{posterior}$) of each pixel size can be computed as shown in Equations 5 and 6, for instances where evidential layers satisfy the conditional independence test [45].

$$\ln\left(O_{posterior}\right) = \ln\left(O(Au_G)\right) + \sum_{i=1}^{n} w_i^k \ (i = 1, 2, 3, \cdots, n) \tag{5}$$

$$w_i^k = \begin{cases} w_i^+; & presence\ of\ the\ ith\ evidential\ layer \\ w_i^-; & absence\ of\ the\ ith\ evidential\ layer \\ 0\ ; & no\ data \end{cases} \tag{6}$$

The metallogenic probability of each pixel is represented as the posterior probability as expressed in Equation 7. The posterior probability is very essential in the characterization of the mineral prospect over an area of interest.

$$P_{posterior} = \frac{O_{posterior}}{1 + O_{posterior}} \tag{7}$$

In order to determine the spatial relationship between the existing Au occurrence and the *ith* class of an evidential layer, the contrast (C) is applicable and expressed in Equation 8. A positive C value stipulates a strong spatial correlation between known Au occurrences and the considered *ith* evidential layer class. Negative C depicts a weak correlation between existing Au occurrences and the considered *ith* evidential layer class. A C value of 0 indicates that the considered *ith* evidential layer class is not relevant for analysis [46].

$$C_i = W_i^+ - W_i^- \tag{8}$$

3.2.2. Information value (IV)

Another bivariate data-driven statistical method whose employability was vital in this study is the information value (IV) technique. Though originally proposed for predictive modeling in geoscience; to make it more flexible for employability in geo-spatial predictive modeling, the IV technique was subsequently modified by [47]. The IV modeling technique thrives on the idea that Au occurrence (Au_G) over an area of interest is influenced by various factors depicted as condition factors or evidential layers (EV_i). For its adaptation in geospatial predictive modeling such as mineral prospectivity modeling, the IV technique can be expressed as shown in Equation 9.

$$IV(AU_G, EV_i) = Log_2\left(\frac{P(Au_G, EV_i)}{P(Au_G)}\right) \tag{9}$$

From Equation 9, $IV\ (Au_G, EV_i)$ represents the information value of various conditioning factors EV_i; $P(Au_G)$ depicts the possibility of occurrence of Au mineral; $P\ (Au_G, EV_i)$ is the possibility of occurrence of Au mineral with respect to an evidential layer EV_i.

The expression in Equation 9 can analogously be expressed in terms of ratios as shown in Equation 10.

$$IV(Au_G, EV_i) = Log_2\left(\frac{Au_G^i / Au_{GT}}{A_{EV}^i / A_T}\right) \tag{10}$$

From Equation 10, Au_G^i represents the Au occurrence areal extent within a selected evidential layer (EV) class; Au_{GT} is the total number of Au occurrence pixels within the EV; A_{EV}^i depicts the area extent of the selected EV class, and AT indicates the total area of the evidential layer.

Results obtained from the computation of the IV values for various classes of evidential layers can be zero, negative or positive. These computed IV values play a primal role in establishing an evidential layer's influence towards Au mineral occurrence within an area of interest. Thus, positive IV values indicate a strong correlation; negative IV values represent a weak correlation whereas zero IV values depict no correlation between existing Au occurrences and the evidential layer used.

3.3. Mineral prospectivity models

By employing the weight of evidence and information value modeling techniques, it was expected that a mineral prospectivity models would

be generated for each of the modeling techniques to characterize the producible zones of Au minerals within the Julie Tenement of Northwestern Ghana. This was preceded by assigning each class of an evidential layer to their respective spatial correlation values by computing by applying the aforementioned data-driven spatial statistical methods (i.e. WofE and IV). The generation of MPM for each of the models used in this study, dwells on the integration of the eleven evidential layers based on their respective attained statistical values as expressed in equation 11 and equation 12 for WofE and IV techniques, respectively.

$$MPM_{WofE} = \sum_{i=1}^{n} (C)_n \quad (11)$$

$$MPM_{IV} = \sum_{i=1}^{n} (IV)_n \quad (12)$$

From Equations 11 and 12, MPM_{WofE} and MPM_{IV} represent, respectively, the mineral prospectivity model generated based on the WofE and IV, respectively. $(C)_n$ and $(IV)_n$, respectively, represent the contrast value and information values obtained for each of the eleven evidential layers employed in this study.

3.4. Validation of mineral prospectivity models

As a rule of thumb and to ensure confidence in the two predictive models generated, they were thus assessed in terms of their prediction efficacy. In view of this, the accuracy of the mineral prospectivity models produced based on the WofE and IV techniques was assessed by employing the receiver operating characteristics (ROC) curve. As it has been found very applicable in assessing various geospatial models in various terranes [16, 43, 48, 49, 50], the ROC curve technique was adopted for this study to determine the performance of mineral prospectivity models that would be generated based on the WofE and IV approaches using the validation dataset comprising 33 existing locations of Au occurrence within the Julie Tenement. The ROC curve generally encompasses an x-axis that depicts the false positive rate values and a y-axis that indicates the true positive rate values. ROC encompasses a range of values from 0.5 to 1; with values nearing 1 adjudged as a representative of a good, predicted model.

4. Results and discussion

4.1. Description of evidential layers

Generation of prospective zones of mineral occurrence encompasses the use of viable factors of essential relevance to the sought-after mineral. Thus, in this study, eleven evidential layers that has been classified based on the natural breaking classification method, and sourced from magnetic, radiometric, geological and geo-chemical datasets were employed. The analytic signal (AS) and the reduction-to-equator (RTE) layers which were sourced from the magnetic data are capable of transforming by removing asymmetric problems associated with magnetic datasets acquired within low magnetic latitude regions [40]. The Julie Tenements, whose mineralization style is associated with quartz-veins and contains sulphide minerals such as arsenopyrite and pyrite, are essential indicators that can be mapped using these two aforementioned magnetic layers [37]. On these maps (shown in Figures 3 and 4), the anomalous regions of high magnetic intensities could be due to the presence of arsenopyrite and pyrite, whose presence in the quartz-veins, are essential indicators of gold mineralization within the studied area. The application of the CET porphyry detection technique on the magnetic data also produced the porphyry density layer, which was essential in delineating porphyry magnetic signatures. The porphyry layer characterizes regions of near-circularly concentric intrusions [51,52], which generally depict high magnetic responses (as shown in Figure 5) and favours mineralization owing to their relationship with deformation. Aside from being generically used for mapping circular features, the porphyry layer is also essential in mapping probable Au porphyries in magnetic terranes. The lineament density layer was deemed relevant in this study because of its significance in mapping regions of abundance structural features of much essence to gold mineralization. The mineralization of the study area, which hinges on the quartz-veins, characterizes various structural features such as dykes and faults (which are depicted on the lineament density layer shown in Figure 6) [37,40]. In general, radiometric layers, which fundamentally comprises the spatial distribution of potassium, thorium, and uranium radioelement concentrations are very important in mapping alteration zones that are essential targets for gold mineralization within the studied area [40]. Thus five layers consisting of potassium (K), thorium (eTh), uranium (eU), potassium-thorium ratio, and

uranium-thorium ratio (shown in Figures 7, 8, 9, 10, and 11) were derived from the radiometric data to complement efforts towards delineating regions of probable mineral prospects within the Julie Tenement. These aforementioned radiometric layers were employed in this study because they are very useful in providing an understanding of various radioelement responses that are associated with the alteration of host rocks as well as mineralization occurrences. In mineralization analysis using radiometrics, a corresponding increase of K and eTh suggests the probable mobilization of gold deposits within systems of hydrothermal alteration. Regions with K increasing and eTh decreasing indicate the prevalence of alteration in ore deposits [53,54]. Also, regions of increased uranium signatures suggest the probable occurrence of mineralization [40] In the delineation of gold mineralization prospects over a region of interest, indicator elements play an enormous role. In this regard, the arsenic concentration layer was derived as a geochemical signature to assist in this study (shown in Figure 12). Arsenic concentration signatures have been observed to demonstrate a relevant association to gold mineralization in various geologic environments [55,56]. In this regard, the use of the arsenic layer furnishes probable essential pathways with gold mineralization occurrences within the study. Geologically, the Julie Tenement is regionally classified into four formations as shown in Figure 13. These four formations include basalts (bas), basalt with magnetite mineralization (bas2), volcano sedimentary rocks (vs) and Granitoid rocks (G2) composed of diorite and tonalitic affinities. The bas, bas2 and vs rocks have all been affected by low-angle thrust faulting forming nappes. The fault planes of these nappes are mapped by shearing usually acting as conduits or pathways for hydrothermal fluids.

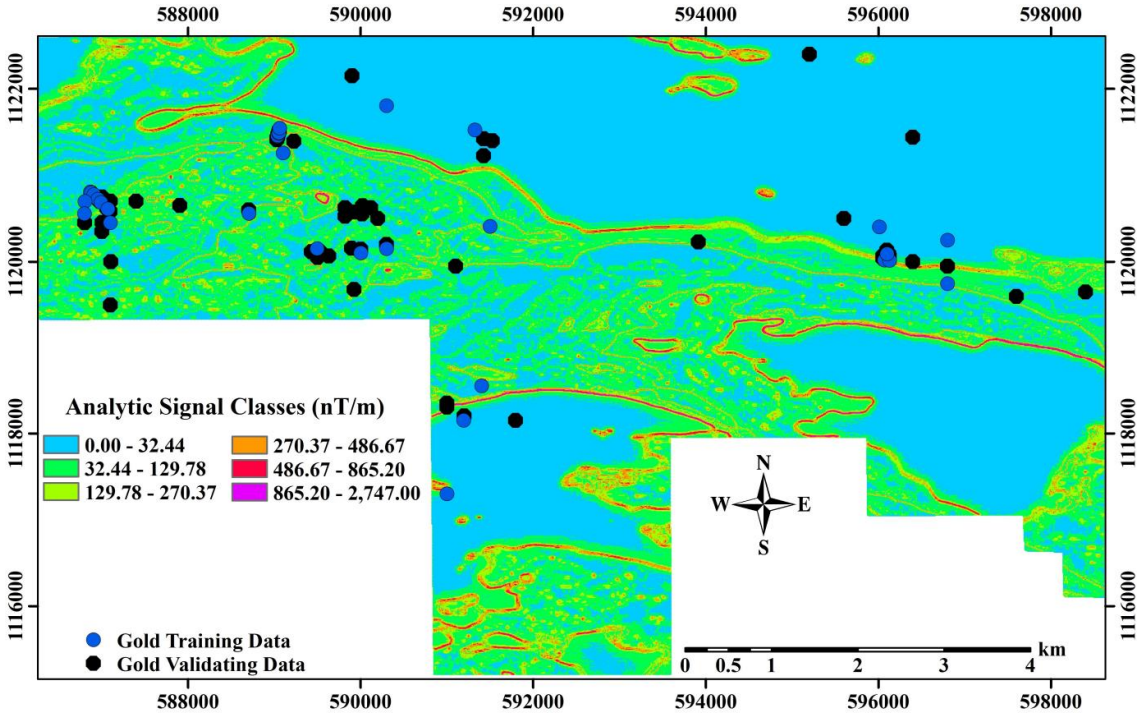

Figure 3. Map of the classified analytic signal layer.

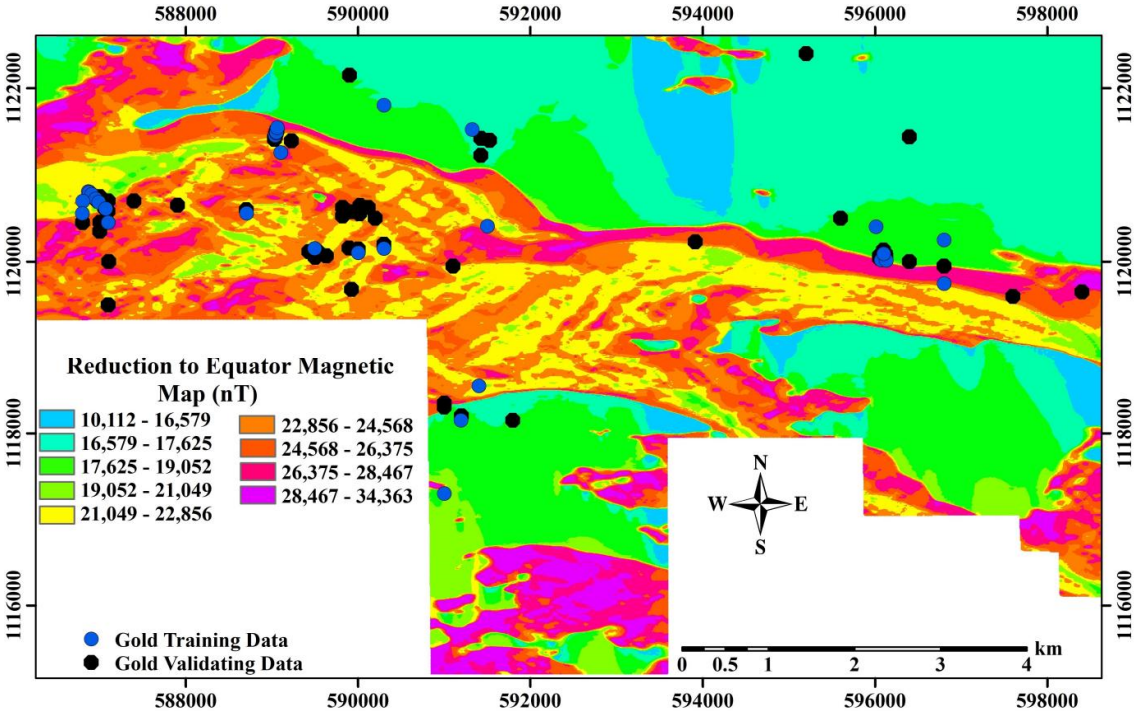

Figure 4. Map of the classified RTE-based magnetic intensity layer.

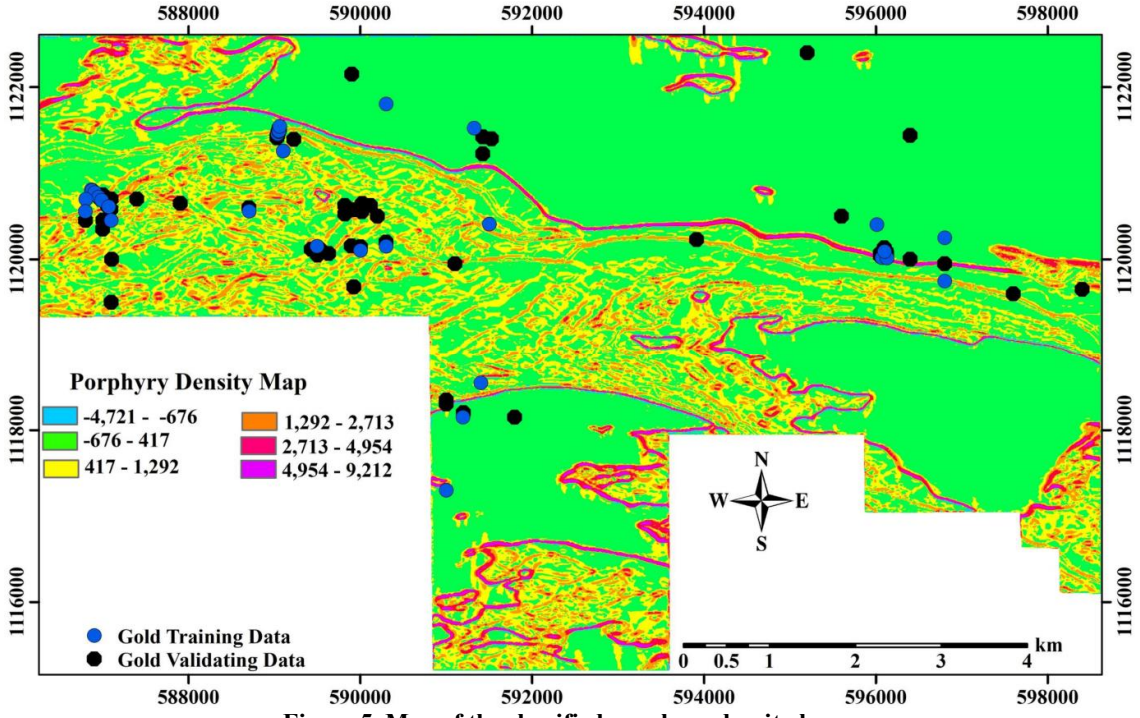

Figure 5. Map of the classified porphyry density layer.

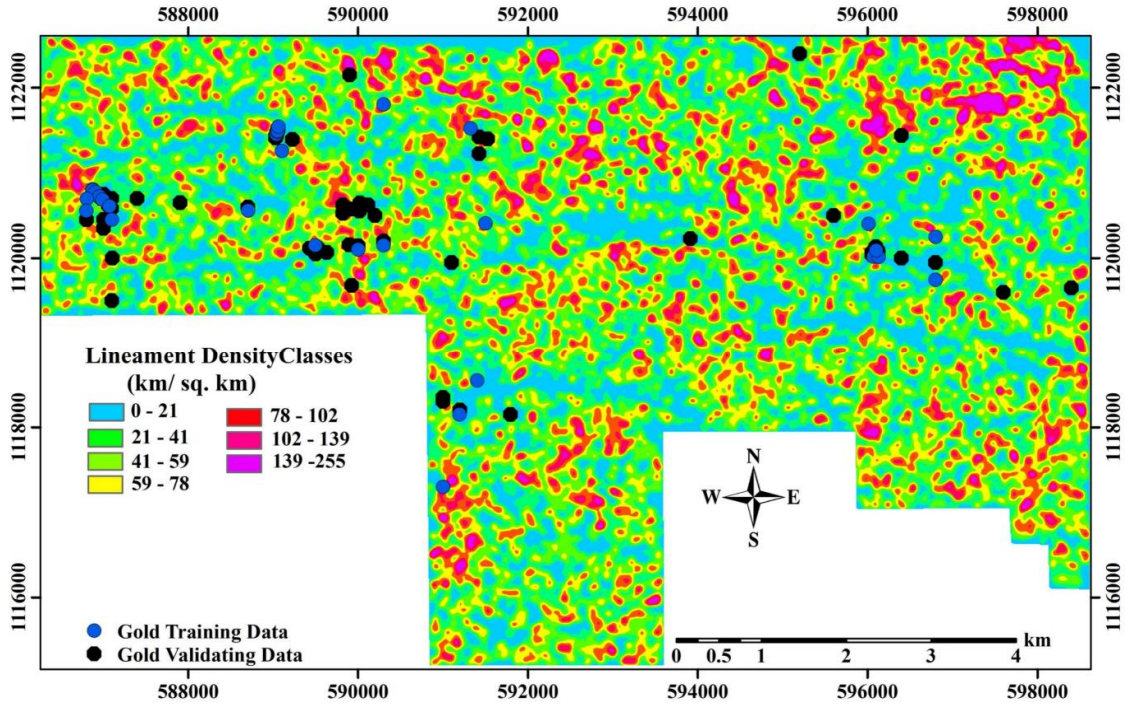

Figure 6. Map of the classified lineament density layer.

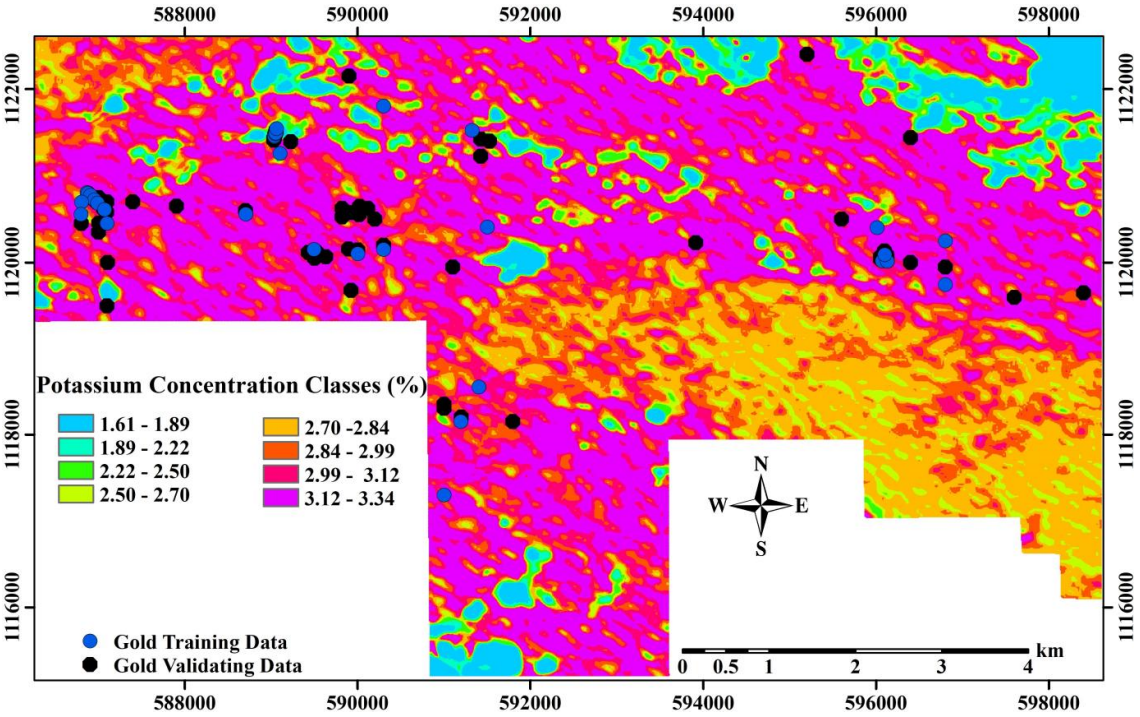

Figure 7. Map of the classified potassium concentration layer.

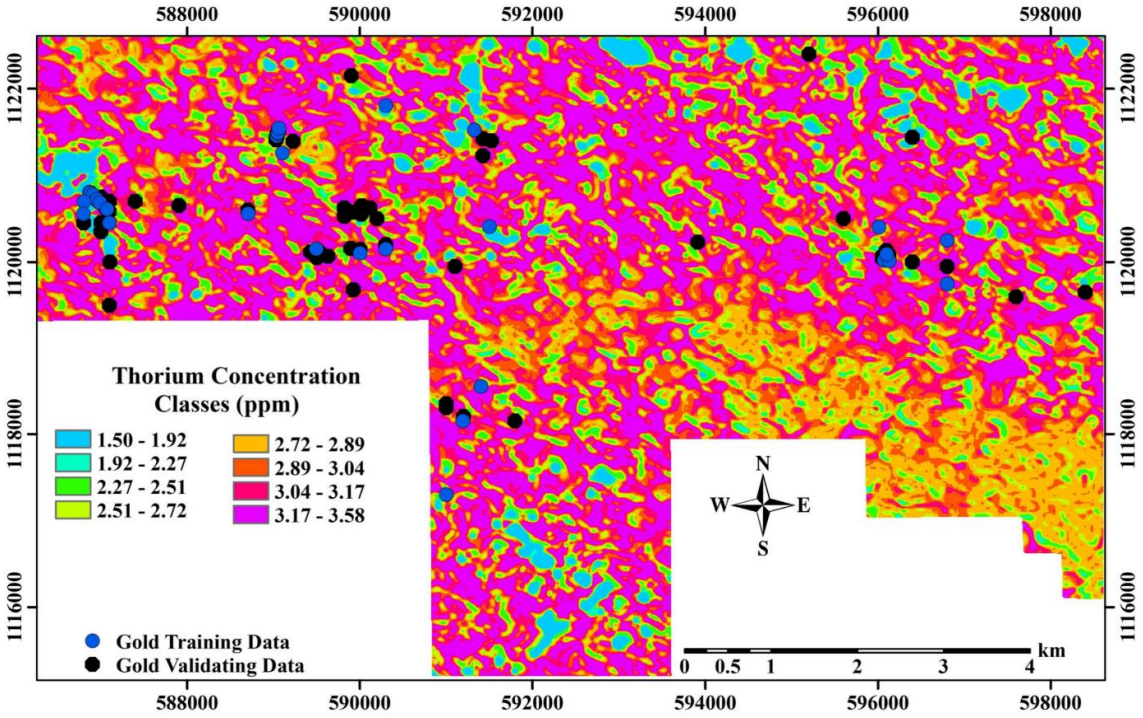

Figure 8. Map of the classified thorium concentration layer.

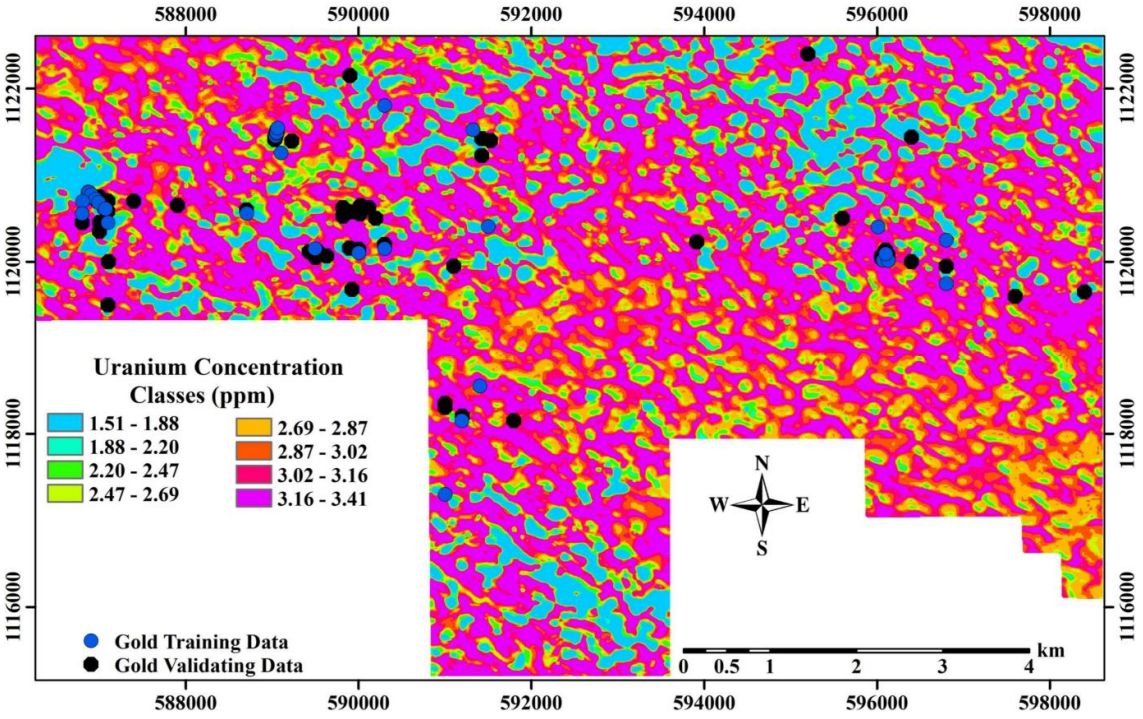

Figure 9. Map of the classified uranium concentration layer.

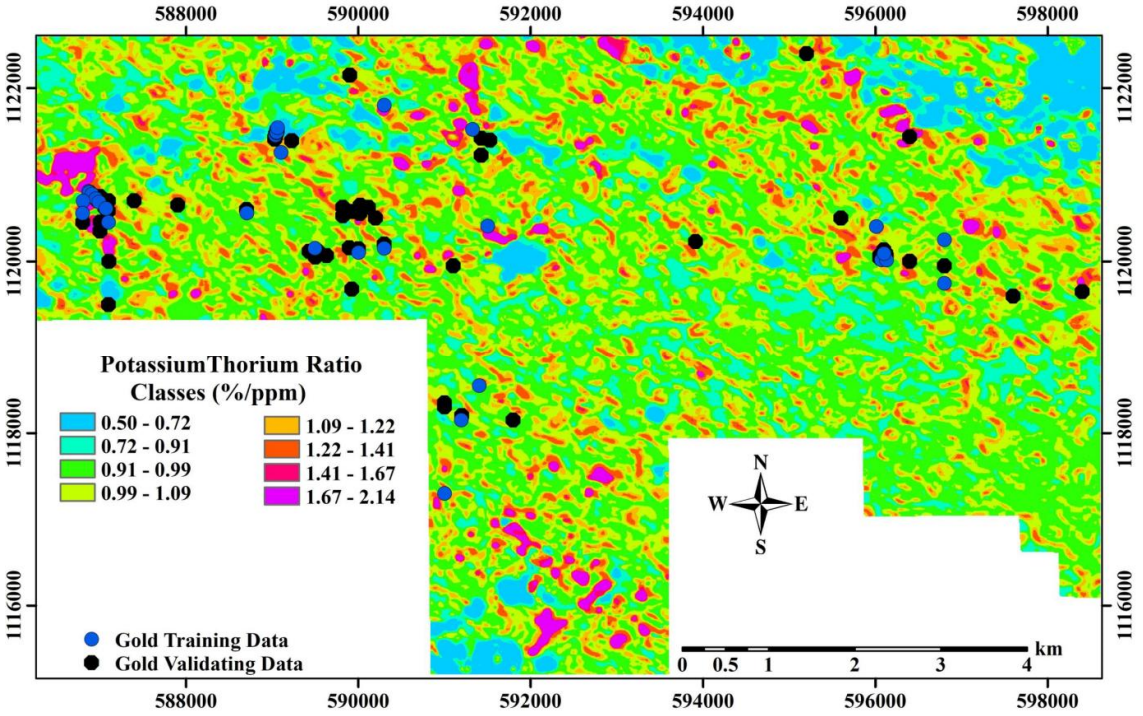

Figure 10. Map of the classified potassium-thorium ratio layer.

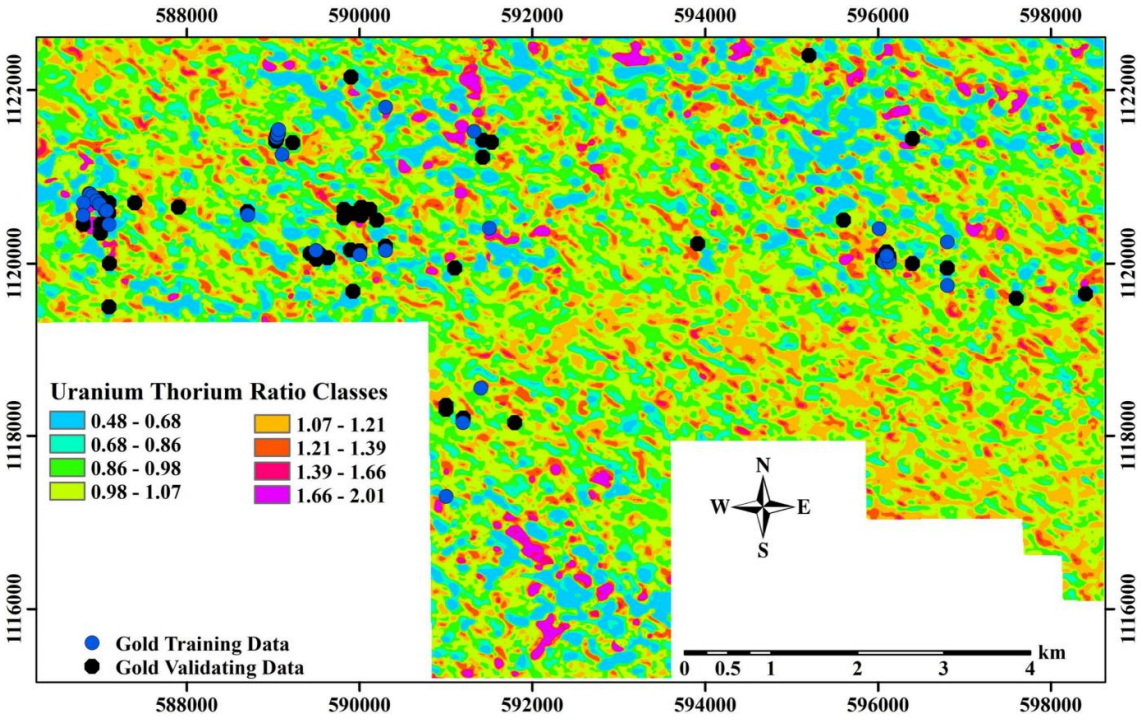

Figure 11. Map of the classified uranium-thorium ratio layer.

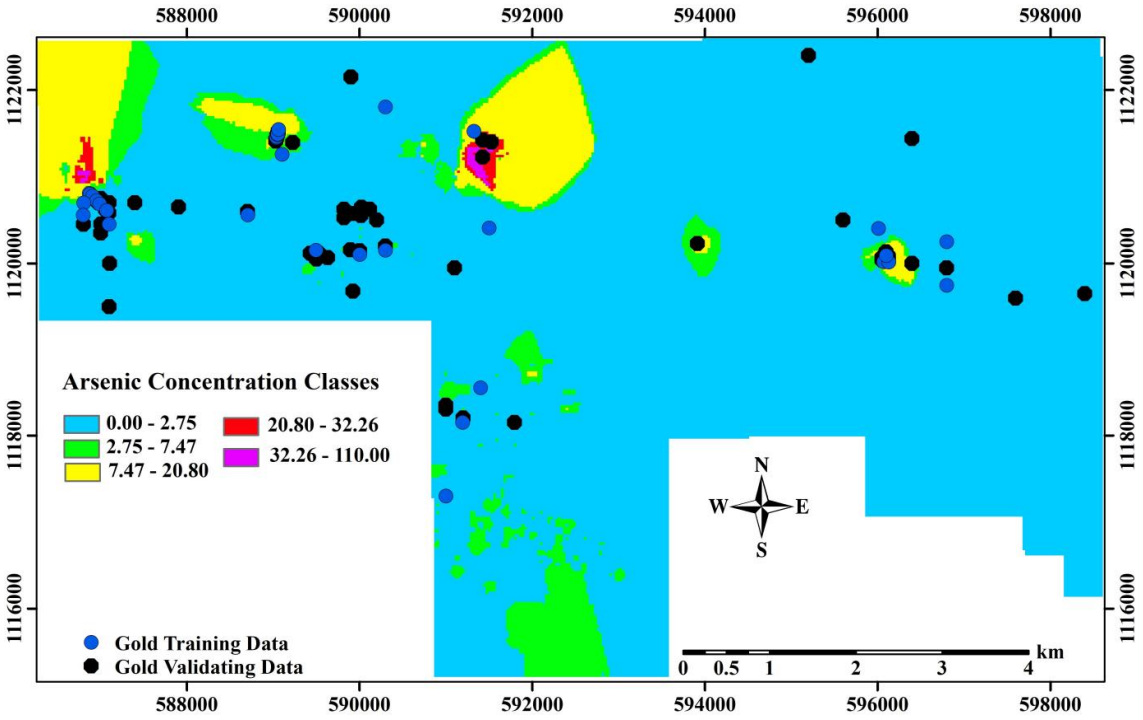

Figure 12. Map of the classified arsenic concentration layer.

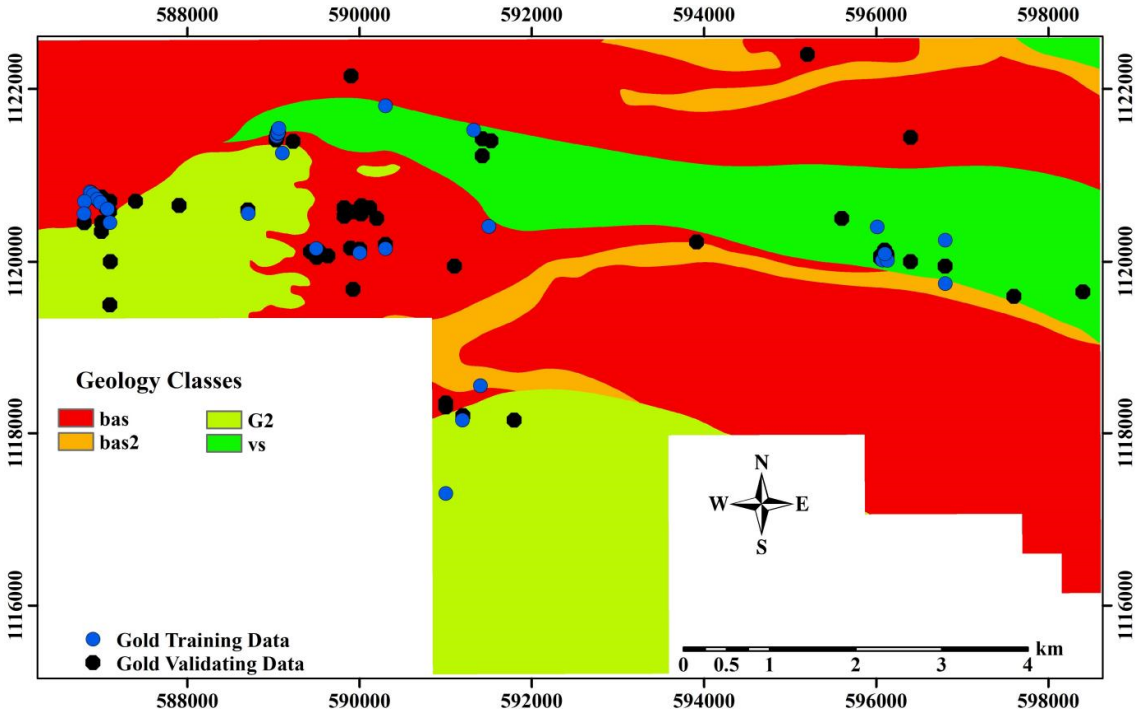

Figure 13. Map of the classified geological layer.

4.2. Spatial analysis of evidential layers with respect to Au occurrences

In this study, the spatial association of each class of the eleven evidential layers were analyzed using the weight of evidence and information value modeling techniques (in Tables 1 and 2). That is to say that for each class of a given evidential layer, the use of the WofE and IV techniques were vital in determining their relevance towards mineral

occurrences within the study area. For the WofE approach, the contrast (*C*) values obtained for each class of an evidential layer (as shown in Tables 1 and 2) were assigned to their respective classes. Synonymously, each evidential layer's class was assigned its respective information value (IV) score. The *C* or IV score obtained for a particular evidential layer's class represents the influence or contribution of the said class towards the mineral prospectivity model to be developed. Generally, a positive *C* or IV score for a particular class indicates that the said class spatial associated with the sought-after mineral occurrence strongly. Negative *C* or IV value depict a weak spatial relation between the class and the sought-after mineral occurrence. In instances where zero (0) values are obtained, it gives an indication that, there is no correlation between the sought-after mineral occurrence and the class, whose spatial correlation has been determined [45,47].

Based on the application of the WofE technique on each of the 4 classes within the geological evidential layer, it was observed that only the vs class, which was deemed to exhibit no meaningful correlation with respect to the known Au occurrence locations within the study area owing to the zero value attained for the weight contrast (*C*). This observation concerning the vs class was also analogously echoed by the information value technique due to the zero-value computed. The three other classes within the geological layer were observed to show strong correlation with the known mineral occurrences within the study area based on both the WofE and IV techniques (shown in Table 1). Thus the bas2 class, followed by the bas class and the G2 class were in descending order, observed to demonstrate strong relevance to Au occurrence within the Julie Tenement with the weight contrast values being 0.648, 0.285, and 0.223 as well as IV scores of 0.2560, 0.0735, and 0.0514, respectively.

For the six classes within the analytic signal layer, only one class with a range of analytical signal-based magnetic intensity values of 0.00 nT m^{-1} - 32.44 nT m^{-1} was observed to demonstrate weakness towards gold mineralization occurrence locations with their computed weight contrast and information value being -1.168 and -0.2842, respectively. Except for the class with analytic signal intensities between 865.20 nT m^{-1} - 2.747.00 nT m^{-1}, which demonstrated no meaningful correlation with the known locations of Au occurrences owing to the unavailability of Au occurrences within the aforementioned class, the four other classes with a range of magnetic intensity values being 32.44 nT m^{-1} - 129.78 nT m^{-1}, 129.78 nT m^{-1} - 270.37 nT m^{-1}, 270.37 nT m^{-1}, - 486.67 nT m^{-1}, and 486.67 nT m^{-1} - 865.20 nT m^{-1} showcased that their respective relationship towards gold mineralization within the study area is strong based on their positive weight contrast scores (0.793, 0.908, 0.043, and 0.536, respectively) and IV scores (0.2053, 0.3522, 0.0185, and 0.2307, respectively) obtained. This subsequently indicates that, within the Julie Tenement, regions with the lowest magnetic intensities have a weak relationship with gold mineralization, whereas the regions having moderate to high magnetic intensities are strongly associated with gold occurrence within the study area.

In the case of the reduction-to-equator (RTE) evidential layer, two out of the three classes (with class ranges of 16,579 nT - 17,625 nT and 17.625 nT - 19.052 nT) with the lowest magnetic intensity values were observed to be characterized by negative values of the weight contrast and information value as shown in Table 2. This is an indication that, the regions with low magnetic intensities within the Julie Tenement are generally not essential pathfinders to gold mineralization. Virtually all RTE classes with moderate to high magnetic intensity values (except one with magnetic intensity range of 28.467nT - 34,363 nT) exhibited a strong relationship towards the gold mineralization occurrences within the study area. This suffices to show that, these highly magnetic regions, which are generally characterized by sulphide-associated indicator minerals such as arsenopyrite and pyrite are very essential towards the gold mineralization prospects of the Julie Tenement [37,40]. For the eight classes of the thorium concentration layer, four of them with concentration values of 2.27 ppm -2.51 ppm, 2.72 ppm - 2.89 ppm, 3.04 ppm - 3.17 ppm, 3.17 ppm - 3.58 ppm with their respective weight contrast and information value scores being (-0.085, -0.445, -0.497, -0.143) and (-0.0349, -0.1685, -0.1771, -0.0448) were observed to be negatively associated with gold occurrence within the study; an indication that these classes are not essential targets for the delineation of the occurrence of gold within the study area. However, the four other classes of thorium concentration (1.50 ppm - 1.92 ppm, 1.92 ppm - 2.27 ppm, 2.51 ppm - 2.72 ppm, and 2.89 ppm - 3.04 ppm) with weight contrast scores of 0.949, 1.415, 0.513, and 0.199 as well as information value scores of 0.3940, 0.5967, 0.1995, and 0.0718, respectively, demonstrated strong correlation to gold mineralization within the Julie

Tenement.

In the case of the uranium concentration layer which comprises eight class ranges, four of these eight classes (1.88 ppm - 2.20 ppm, 2.20 ppm - 2.47 ppm, 12.47 ppm - 2.69 ppm, and 2.69 ppm - 2.87 ppm) demonstrated weakness towards the known locations of gold occurrences within the study area based on their weight contrast (respectively -0.496, -1.989, -1.931, and -0.372) and information value scores (-0.1975, -0.7671, -0.6975, and -0.1390, respectively) computed. With the exception of eU concentration class range of 1.51 ppm - 1.88 ppm (which is characterized by low concentration values of uranium but still exhibited strong association towards gold mineralization with IV and *C* scores of 0.2578 and 0.675), all the other uranium concentration class ranges, which exhibited strong coherence with known locations of gold occurrence (2.87 ppm - 3.02 ppm, 3.02 ppm - 3.16 ppm, and 3.16 ppm - 3.41 ppm) based on their respective weight contrast (0.919, 2.552 and 3.301) and information value scores (0.3597, 1.0458, and 1.3054) were of high eU concentration. This observation further corroborates with the literature assertion that high uranium concentrations exhibit strong coherence with gold mineralization within an area of interest [40].

The potassium evidential layer, which was also discretized into eight classes with various ranges of concentration (in percentage), were analyzed to ascertain the geospatial association between each of these eight classes and gold mineralization occurrence. Two potassium concentration classes (2.99% - 3.12%, and 3.12% - 3.31%) exhibited no correlation towards mineralization within the study area.

With the other six potassium concentration classes, only one (1.89% - 2.22%) was observed to show weakness towards gold mineralization occurrence within the study area due to the negative score obtained for the IV (-0.2854) and *C* (-0.668). Thus in all, five classes of the potassium evidential layers were observed to have demonstrated positive coherence with respect to gold mineralization occurrence within the Julie Tenement based on their IV and *C* scores (as shown in Table 2).

For the uranium-thorium ratio evidential layer, two classes (with ratio score ranges of 1.39 - 1.66 and 1.66 -2.01) were observed to have zero scores for the weight contrast and information value. Two other classes with range of values comprising 10.48 - 0.68 and 1.21 - 1.39 were, however, found to associate with gold mineralization occurrence weakly owing to the negatively computed *C* and IV scores as shown in Table 1. The four other classes of uranium-thorium ratio layer exhibited a strong correlation towards the known Au locations within the study area.

The potassium-thorium layer, which also comprises eight classes was observed to be characterized by three classes that demonstrated weakness towards gold mineralization within the Julie Tenement (shown in Table 1). The five other classes of the K-eTh ratio layer exhibited a strong correlation towards the known gold occurrences within the tenement owing to the positive scores attained for both the IV and *C*. With the exception of only one K-eTh ratio class (0.50 %/ppm - 0.72 %/ ppm, which exhibited a positive correlation with the known Au occurrences, although it had the smallest K-eTh ratio value), all the other four classes with a strong association with known Au occurrence location were characterized by high K-eTh ratio scores. Thus, these four classes with positive IV and *C* further demonstrate the existence of mineralized systems associated with potassium metasomatism within the aforementioned classes [40, 57].

Among the six classes within the porphyry density evidential layer, two (-676 – 417, and 4,954 - 9,212) weakly correlated with the gold mineralization occurrences within the study area. The four other classes within the porphyry layer were observed to have demonstrated a positive correlation towards gold mineralization occurrence within the tenement as shown in Table 2. In the case of the lineament density evidential layer, only one class (139- 255 km/sq.km) showed no correlation with respect to the known Au occurrences, because of the unavailability of any known Au occurrence within the study area. Also, three classes of lineament density values (21 km/sq.km - 78 km/sq.km) were observed to show a weak correlation with the known Au locations based on the negative scores IV and C scores. Two of the classes with high lineament density (78 km/sq.km - 102 km/sq.km, and 102 km/sq.km - 139 km/sq.km) were observed to exhibit strong spatial association with gold occurrences within the studied area. The arsenic concentration layer, which comprises five classes, was analyzed using the weight of evidence and the information value techniques. Two of these classes with concentration ranges of 0.00 - 2.75 ppm and 2.75 ppm - 7.47 ppm demonstrated weak association towards the known locations of Au occurrences within the studied area due to the negative *C* and IV scores attained as shown in Table 2. The three classes with high

arsenic concentration values (7.47 ppm - 20.80 ppm, 20.80 ppm - 32.26 ppm, and 32.26 ppm - 110.00 ppm) were observed to have positive scores for the weight contrast (1.780, 1.155, and 1.737, respectively) and the information value (0.7226, 0.4648, and 0.7150, respectively) - an indication of a strong correlation between the known locations of gold occurrences and the highly concentrated arsenic regions zones within the study area; an assertion that corroborates with relevant literature that concerns arsenic-gold relationship [55,56].

4.3. Mineral prospectivity models

In order to create a predictive model that outlines variously prospective zones over the Julie Tenement in the northwestern part of Ghana, the two data-driven modeling methods comprising the weight of evidence and the information value were employed. In the case of the Wof E techniques, the classified evidential layers with their respective *C* values assigned were synthesized based on the weight contrast as shown in Equation 11 to generate a Wof E-based mineral prospectivity map (shown in Figure 14). For the information value modeling technique, Equation 12 was employed to integrate all the IV score-assigned evidential layers to generate an IV-based mineral prospectivity model (shown in equation 15). These two predictive models (shown in Figures 14 and 15) generated were classified into (1) areas with the lowest gold prospect (referred to as "Very Low"), (2) regions with low mineral prospects (denoted by "Low"), (3) regions with moderate prospect to gold mineralization (depicted as "Moderate") (4) zones with moderately high mineral potential (known as "Moderately High") and (5) areas with the highest gold prospects (depicted as "High") within the study area. The "Very Low", "Low", and "Moderate" regions of gold potential covering area sizes of respectively 8.08 km^2, 12.98 km^2, and 17.18 km^2 for the W of E-based MPM and 8.78 km^2, 14.09 km^2 and 17.69 km^2 for IV-based MPM. These "Very Low", "Low", and "Moderate" regions were generally observed to be characterized by low to moderate magnetic intensities on the RTE layer and low porphyry density. The regions with "Moderately High" and "High" mineral prospects, were respectively observed to cover an areal size of 14.58 km^2 and 8.23 km^2 for the W of E-based MPM and 12.30 km^2 and 8.19 km^2 for the IV-based MPM (shown in Table 3). These aforementioned high regions of gold mineralization occurrence within the study area generally coincided with regions of high magnetic intensity on the RTE layer, high potassium concentration and high porphyry density. Geologically, these highly prospective zones of gold mineralization were delineated within (a) the centrally-lying bas formation and the western part of the northward-lying bas formation (b) the centrally-lying bas2 formation and southern part of the southwardly-lying G2 formation within the study area. Gold prospect within the study area was generally low within the vs formation. It is also noteworthy that the predominance of basalts, which are fine-grained extrusive rocks characterized by smaller features of smaller lava-rich features as well as clays (which were well elucidated by the radiometric layers) within the study area contributed extensively to the mottled patterns observed in the models produced (i.e. Figures 14 and 15).

Table 1. Information value and weight contrast scores obtained for various classes of evidential layers (EVs) used.

EVs	Class	Total number of pixels	Au occurrence pixels	IV	*W*+	*W*−	*C*
Geological layer	bas	3688749	437	0.0514	0.118	-0.167	0.285
	bas2	437404	83	0.256	0.59	-0.058	0.648
	G2	1492295	186	0.0735	0.169	-0.054	0.223
	vs	1090113	0	0	0	0	0
Analytical signal Layer (nT m^{-1})	0.00 - 32.44	3912147	214	-0.2842	-0.654	0.514	-1.168
	32.44 - 129.78	2090537	353	0.2053	0.473	-0.32	0.793
	129.78 - 270.37	468733	111	0.3522	0.811	-0.097	0.908
	270.37 - 486.67	173030	19	0.0185	0.042	-0.001	0.043
	486.67 - 865.20	50273	9	0.2307	0.531	-0.005	0.536
	865.20 -2747.00	13841	0	0	0	0	0
Thorium concentration layer (ppm)	1.50 - 1.92	180289	47	0.394	0.907	-0.042	0.949
	1.92 - 2.27	88988	37	0.5967	1.374	-0.041	1.415
	2.27 - 2.51	380958	37	-0.0349	-0.08	0.005	-0.085
	2.51 - 2.72	558236	93	0.1995	0.459	-0.054	0.513
	2.72 - 2.89	1036424	74	-0.1685	-0.388	0.057	-0.445
	2.89 - 3.04	1047083	130	0.0718	0.165	-0.034	0.199
	3.04 - 3.17	1457065	102	-0.1771	-0.408	0.089	-0.497
	3.17 - 3.58	1959518	186	-0.0448	-0.103	0.04	-0.143
Uranium-thorium ratio layer	0.48 - 0.68	611651	56	-0.0605	-0.139	0.013	-0.152
	0.68 - 0.86	160085	74	0.6427	1.48	-0.087	1.567
	0.86 - 0.98	334918	186	0.7224	1.664	-0.255	1.919
	0.98 - 1.07	417473	214	0.6876	1.584	-0.297	1.881
	1.07 - 1.21	709775	148	0.297	0.684	-0.123	0.807
	1.21 - 1.39	891306	28	-0.525	-1.209	0.102	-1.311
	1.39 - 1.66	1351632	0	0	0	0	0
	1.66 - 2.01	2231721	0	0	0	0	0
Uranium concentration layer (ppm)	1.51 - 1.88	587862	112	0.2578	0.594	-0.081	0.675
	1.88 - 2.20	688866	46	-0.1975	-0.455	0.041	-0.496
	2.20 - 2.47	1556223	28	-0.7671	-1.766	0.223	-1.989
	2.47 - 2.69	2178232	46	-0.6975	-1.606	0.325	-1.931
	2.69 - 2.87	1099329	84	-0.139	-0.32	0.052	-0.372
	2.87 - 3.02	423344	102	0.3597	0.828	-0.091	0.919
	3.02 - 3.16	87220	102	1.0458	2.409	-0.143	2.552
	3.16 - 3.41	87485	186	1.3054	3.008	-0.293	3.301
Potassium-thorium ratio layer (%/ppm)	0.50 - 0.72	392329	65	0.1971	0.454	-0.036	0.49
	0.72 - 0.91	774131	19	-0.6322	-1.456	0.095	-1.551
	0.91 - 0.99	2502189	177	-0.1725	-0.397	0.178	-0.575
	0.99 - 1.09	1751509	139	-0.1226	-0.282	0.083	-0.365
	1.09 - 1.22	737116	167	0.333	0.767	-0.153	0.92
	1.22 - 1.41	373915	56	0.1532	0.353	-0.025	0.378
	1.41 - 1.67	65130	46	0.8268	1.904	-0.058	1.962
	1.67 - 2.14	112242	37	0.4959	1.142	-0.037	1.179

Table 2. Information value and weight contrast scores obtained for various classes of evidential layers (EVs) used continued.

EVs	Class	Total number of pixels	Au occurrence pixels	IV	*W+*	*W−*	*C*
Porphyry density layer	-4,721 - -676	40407	9	0.7497	0.75	-0.007	0.757
	-676-417	4558977	288	-0.5104	-0.51	0.614	-1.124
	417 - 1,292	1329866	242	0.5476	0.548	-0.199	0.747
	1,292 - 2,713	508789	130	0.887	0.887	-0.125	1.012
	2,713 - 4,954	164287	28	0.4821	0.482	-0.016	0.498
	4,954 - 9,212	106235	9	-0.2169	-0.217	0.003	-0.22
Potassium concentration layer (%)	1.61 - 1.89	307154	56	0.2387	0.55	-0.036	0.586
	1.89 - 2.22	146656	8	-0.2854	-0.657	0.011	-0.668
	2.22 - 2.50	176906	19	0.0088	0.02	-0.001	0.021
	2.50 - 2.70	323697	56	0.2159	0.497	-0.033	0.53
	2.70 - 2.84	1002080	223	0.3252	0.749	-0.218	0.967
	2.84 - 2.99	944669	344	0.5391	1.242	-0.516	1.758
	2.99 - 3.12	1389826	0	0	0	0	0
	3.12 - 3.34	2417573	0	0	0	0	0
RTE layer (nT)	10,112 - 16,579	286752	56	0.2685	0.618	-0.039	0.657
	16,579 - 17,625	1744862	121	-0.1812	-0.417	0.113	-0.53
	17,625 - 19,052	1210221	37	-0.5368	-1.236	0.145	-1.381
	19,052 - 21,049	344988	186	0.7095	1.634	-0.253	1.887
	21,049 - 22,856	802296	139	0.2165	0.499	-0.092	0.591
	22,856 - 24,568	847731	130	0.1635	0.377	-0.068	0.445
	24,568 - 26,375	727781	37	-0.316	-0.728	0.061	-0.789
	26,375 - 28,467	540063	0	0	0	0	0
	28.467 - 34,363	203867	0	0	0	0	0
Lineament density layer (km/sq.km)	0 - 21	1126308	242	0.31	0.714	-0.236	0.95
	21 - 41	1660824	139	-0.0995	-0.229	0.065	-0.294
	41 - 59	1614499	111	-0.1849	-0.426	0.104	-0.53
	59 - 78	1209899	84	-0.1806	-0.416	0.072	-0.488
	78 - 102	722625	84	0.0432	0.099	-0.013	0.112
	102 - 139	303325	46	0.1587	0.365	-0.021	0.386
	139 - 255	71081	0	0	0	0	0
Arsenic concentration layer (ppm)	0.00 - 2.75	4990401	399	-0.1193	-0.275	0.529	-0.804
	2.75 - 7.47	1141519	56	-0.3315	-0.763	0.104	-0.867
	7.47 - 20.80	167386	93	0.7226	1.664	-0.116	1.78
	20.80 - 32.26	273721	84	0.4648	1.07	-0.085	1.155
	32.26 - 110.00	135534	74	0.715	1.647	-0.09	1.737

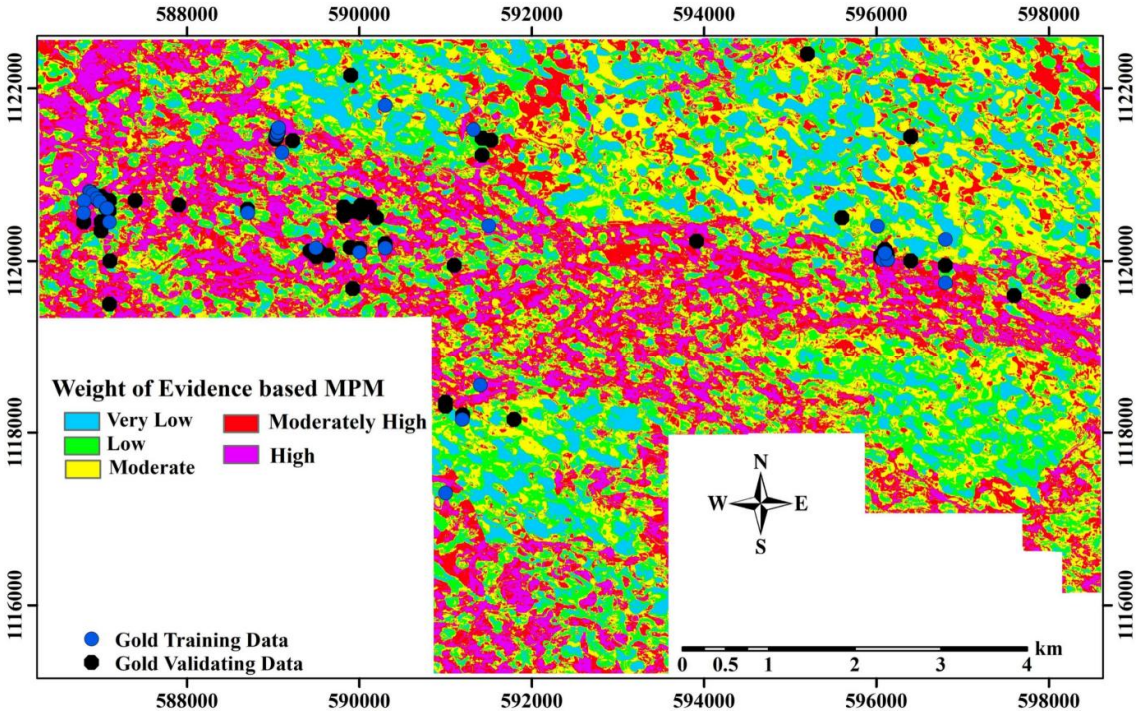

Figure 14. Weight of evidence-based mineral prospectivity model.

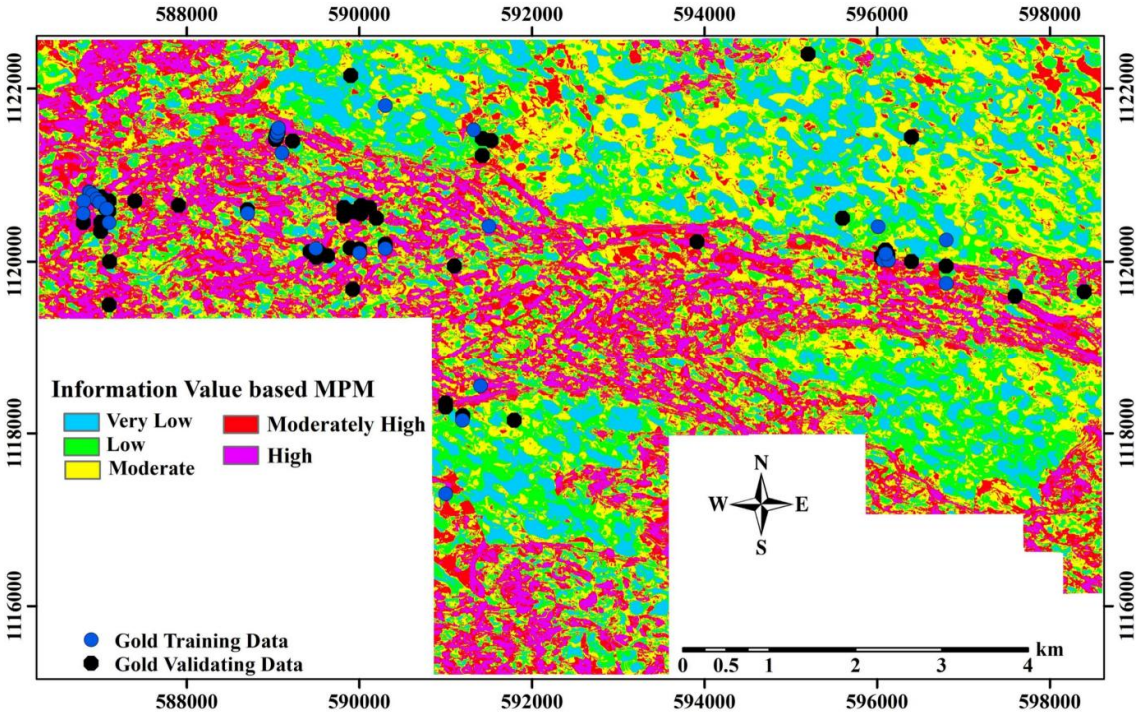

Figure 15. Information value-based mineral prospectivity model.

Table 3. Area extent and percentage of mineral prospectivity classes.

MPM	Weight of evidence		Information Value	
class	Area of class (km^2)	Percentage (%)	Area of class (km^2)	Percentage (%)
Very Low	8.08	13.24	8.78	14.38
Low	12.98	21.26	14.09	23.08
Moderate	17.18	28.14	17.69	28.98
Moderately High	14.58	23.88	12.3	20.15
High	8.23	13.48	8.19	13.41

4.4. Evaluation of mineral prospectivity models

In order to quantitatively evaluate and compare the predictive mineral models generated based on the WofE and IV techniques, the receiver operating characteristics (ROC) curve evaluation technique was employed. In the use of the ROC curve for the WofE-based MPM (shown in Figure 16(a)) and IV-based MPM (shown in Figure 16(b)), the horizontal axes depicted the false positive rate, which concerns situations where an area is predicted to be highly prospective of gold mineralization within the study area when in actual fact, that region is not highly prospective. The vertical axes are represented as true positives, which is the probability that an area delineated or predicted as highly prospective to gold mineralization is actually high in terms of gold mineralization within the study area. The ROC score, which determines the efficacy of a particular model produced for the WofE-based MPM and the IV-based MPM were respectively 0.743 and 0.751. These ROC scores (both of which are greater than 0.7) obtained for each of the two models indicate that the models are efficiently generated. However, by comparing the two ROC scores obtained, it can be inferred that the mineral prospectivity model produced by incorporating the information value technique is more efficient (ROC score of 0.751) than that obtained for MPM generated based on the weight of evidence.

The validity of the outputs generated for the mineral prospectivity models shown in Figures 11 and 12 was further assessed by qualitatively determining how the delineated highly prospective zones correlate with various mineralized lithological classes. Mineral exploration activities carried out by Amponsah et al. [35] and Resources Limited [4], stipulates that gold mineralization occurrence in the Julie tenement is prevalent within lithological classes comprising basalts (bas and bas2) and granitoids (G2). From the MPM outputs shown in Figures 11 and 12, the moderately high and high prospectivity classes were generally observed to be associated with G2 and bas lithological formation within the central, western, and the southern part of the studied area. The northern part of the studied area (characterized by basalts), is however characterized by moderate to moderately high prospectivity output. In the volcanosedimentary (vs) rock formation, prospectivity outputs observed were generally low to moderate. These outputs further corroborate with literature that, gold mineralization within the Julie is strongly associated with the basalts and the granitoids but low within the volcanosedimentary (vs) rocks [4,35].

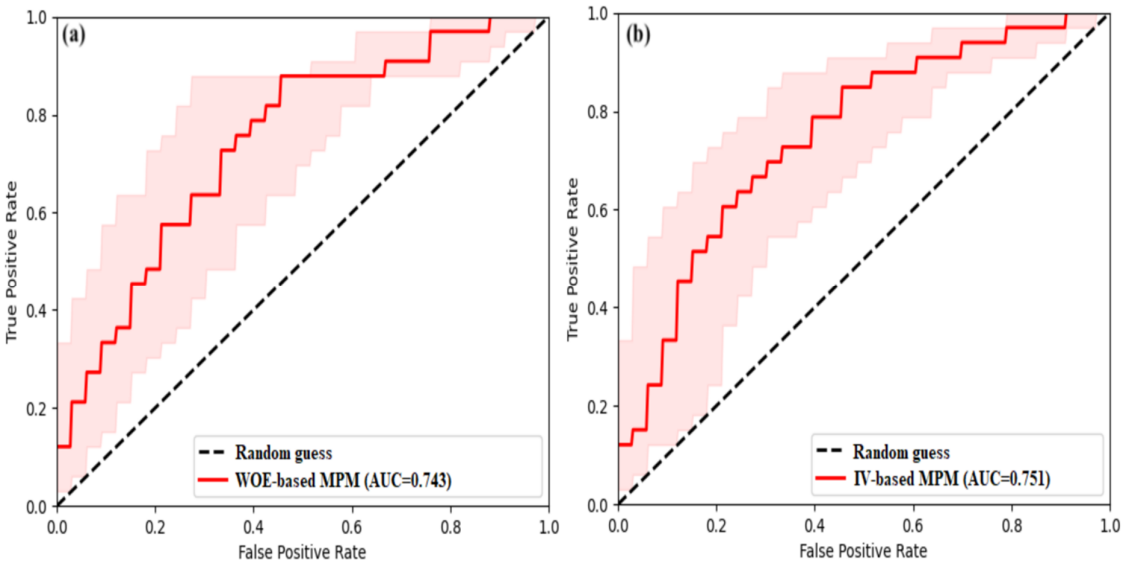

Figure 16. Receiver operating characteristics (ROC) curve for (a) WOE-based MPM (b) IV-based MPM.

5. Conclusions

The main objective of this study was to employ bivariate data-driven statistical techniques to map out prospective zones of mineralization occurrences within the Julie Area of Northwestern Ghana. In carrying out this task, an essential stage that ought not to be overlooked is the selection conditioning factors and thus eleven factors (geo-scientific evidential layers) were properly selected as input layers for carrying out the aforementioned objective. By applying two data-driven statistical techniques (weight of evidence and information value), two predictive models characterizing various classes of gold mineralization prospects within the study area were produced. The information value-based mineral prospectivity model was discretized into five classes of very low, low, moderate, high and high prospective zones with area coverage of 8.78 km^2, 14.09 km^2, 17.69 km^2, 12.30 km^2, and 8.19 km^2, respectively. In the case of the mineral prospectivity model generated based on the weight of evidence approach, the very low, low, moderate, high, and high mineral potential zones were delineated to cover respective areas of 8.08 km^2, 12.98 km^2, 17.18 km^2, 14.58 km^2, and 8.23 km^2, respectively. To make these IV-based and WofE-based predictive models worthy for consideration by mineral exploration geoscientists during exploration programs within the studied area, a standard statistical and commonly used validation technique known as the receiver operating characteristics (ROC) curve was used to assess and evaluate the accuracy of the models produced. The area under ROC curve (AUC) scores obtained for the IV-based MPM and the WofE-based MPM were 0.751 and 0.743, respectively. This suffices to show that the accuracy of the IV-based MPM is higher than the WofE-based MPM created. It is noteworthy that both the IV-based MPM and WofE-based MPM produced good results (with AUC scores greater than 0.7), and thus can be used as essential models to guide viable for unraveling the mineral prospects within the northwestern Ghana. Also, from the outputs obtained, the IV and WofE techniques can be said to be viable methods that can be used for the generation of geospatially-based predictive models in other geological terranes.

References

[1]. Bridge, G. (2004). Mapping the bonanza: geographies of mining investment in an era of neoliberal reform. *The Professional Geographer*, *56(3)*, 406–421.

[2]. Hilson, G. and Banchirigah, S. M. (2009). Are alternative livelihood projects alleviating poverty in mining communities? experiences from Ghana. *The Journal of Development Studies*, *45(2)*, 172–196.

[3]. Forson, E. D., Menyeh, A., Wemegah, D. D., Danuor, S. K., Adjovu, I., and Appiah, I. (2020). Mesothermal gold prospectivity mapping of the southern Kibi-Winneba belt of Ghana based on fuzzy analytical hierarchy process, concentration-area (ca) fractal model and prediction-area (pa) plot. *Journal of Applied Geophysics*, *174*, 103971.

[4]. Azumah Resources Limited (2018). *The Julie Mineral Resource Estimate*. Unpublished internal report.

[5]. Sun, T., Chen, F., Zhong, L., Liu, W., and Wang,

Y. (2019). Gis-based mineral prospectivity mapping using machine learning methods: A case study from tongling ore district, eastern china. *Ore Geology Reviews*,*109,* 26–49.

[6]. Ma, Y., Zhao, J., Sui, Y., Liao, S., and Zhang, Z. (2020). Application of knowledge-driven methods for mineral prospectivity mapping of polymetallic sulfide deposits in the southwest indian ridge between 46° and 52° E. *Minerals*, *10(11)*, 970.

[7]. Riahi, S., Bahroudi, A., Abedi, M., Aslani, S., and Elyasi, G.-R. (2021). Integration of airborne geophysics and satellite imagery data for exploration targeting in porphyry Cu systems: Chahargonbad district, Iran. *Geophysical Prospecting*, *69(5)*, 1116–1137.

[8]. Forson, E. D. and Menyeh, A. (2023). Best worst method-based mineral prospectivity modeling over the central part of the southern Kibi-Winneba belt of Ghana. *Earth Science Informatics*, *16(2)*, 1657–1676.

[9]. Abedi, M., Torabi, S. A., Norouzi, G.-H., and Hamzeh, M. (2012). Electre iii: A knowledge-driven method for integration of geophysical data with geological and geochemical data in mineral prospectivity mapping. *Journal of applied geophysics*, *87*, 9–18.

[10]. Daviran, M., Parsa, M., Maghsoudi, A., and Ghezelbash, R. (2022). Quantifying uncertainties linked to the diversity of mathematical frameworks in knowledge-driven mineral prospectivity mapping. *Natural Resources Research*, *31(5)*, 2271–2287.

[11]. Li, H., Li, X., Yuan, F., Jowitt, S. M., Dou, F., Zhang, M., Li, X., Li, Y., Lan, X., Lu, S. (2022). Knowledge-driven based three-dimensional prospectivity modeling of Fe–Cu skarn deposits; a case study of the fanchang volcanic basin, anhui province, eastern china. *Ore Geology Reviews*, page 105065.

[12]. Sabbaghi, H. and Tabatabaei, S. H. (2022). Application of the most competent knowledge-driven integration method for deposit-scale studies. *Arabian Journal of Geosciences*, *15(11)*, 1–10.

[13]. Carranza, E., Hale, M., and Faassen, C. (2008). Selection of coherent deposit-type locations and their application in data-driven mineral prospectivity mapping. *Ore geology reviews*, *33(3-4)*, 536–558.

[14]. Bai, H., Cao, Y., Zhang, H., Wang, W., Jiang, C., and Yang, Y. (2022). Applying data-driven-based logistic function and prediction-area plot to map mineral prospectivity in the qinling orogenic belt, central china. *Minerals*, *12(10)*, 1287.

[15]. Forson, E. D., Wemegah, D. D., Hagan, G. B., Appiah, D., Addo-Wuver, F., Adjovu, I., Otchere, F. O., Mateso, S., Menyeh, A., and Amponsah, T. (2022). Data-driven multi-index overlay gold prospectivity mapping using geophysical and remote sensing datasets. *Journal of African Earth Sciences*, *190*, 104504.

[16]. Zhang, S., Carranza, E. J. M., Xiao, K., Wei, H., Yang, F., Chen, Z., Li, N., and Xiang, J. (2022). Mineral prospectivity mapping based on isolation forest and random forest: Implication for the existence of spatial signature of mineralization in outliers. *Natural Resources Research*, *31(4)*, 1981–1999.

[17]. Zhang, Z., Wang, G., Carranza, E. J. M., Fan, J., Liu, X., Zhang, X., Dong, Y., Chang, X., and Sha, D. (2022). An integrated framework for data-driven mineral prospectivity mapping using bagging-based positive-unlabeled learning and Bayesian cost-sensitive logistic regression. *Natural Resources Research*, pages 1–20.

[18]. Amponsah, P. O. and Forson, E. D. (2023). Geospatial modelling of mineral potential zones using data-driven based weighting factor and statistical index techniques. Journal of African Earth Sciences, *206*, 105020.

[19]. Harris, J., Grunsky, E., Behnia, P., and Corrigan, D. (2015). Data-and knowledge-driven mineral prospectivity maps for canada's north. *Ore Geology Reviews*, *71*, 788–803.

[20]. Zhang, N. and Zhou, K. (2015). Mineral prospectivity mapping with weights of evidence and fuzzy logic methods. *Journal of Intelligent & Fuzzy Systems*, *29(6)*, 2639–2651.

[21]. Chudasama, B., Torppa, J., Nykänen, V., Kinnunen, J., Lerssi, J., and Salmirinne, H. (2022). Target-scale prospectivity modeling for gold mineralization within the rajapalot au-co project area in northern Fennoscandian shield, finland. part 1: application of knowledge-driven-and machine learning-based-hybrid-expert systems for exploration targeting and addressing model-based uncertainties. *Ore Geology Reviews*, page 104937.

[22]. Salvi, S., Amponsah, P. O., Siebenaller, L., Béziat, D., Baratoux, L., and Jessell, M. (2016). Shear-related gold mineralization in northwest ghana: The julie deposit. *Ore Geology Reviews*, *78*, 712–717.

[23].
Bourenane, H., Guettouche, M. S., Bouhadad, Y., and Braham, M. (2016). Landslide hazardmapping in the Constantine city, northeast Algeria using frequency ratio, weighting factor, logistic regression, weights of evidence, and analytical hierarchy process methods. *Arabian Journal of Geosciences, 9(2)*, 1–24.

[24]. Dickson, K. and Benneh, G. (1988). A new geography of Ghana: Longman group UK limited.

[25]. Feybesse, J.-L., Billa, M., Guerrot, C., Duguey, E., Lescuyer, J.-L., Milesi, J.-P., and Bouchot, V. (2006). The Paleoproterozoic Ghanaian province: geodynamic model and ore controls, including regional stress modeling. *Precambrian Research, 149(3-4)*, 149–196.

[26]. Jessell, M. W., Amponsah, P. O., Baratoux, L., Asiedu, D. K., Loh, G. K., and Ganne, J. (2012). Crustal-scale transcurrent shearing in the

Paleoproterozoic Sefwi-Sunyani-Comoe region, West Africa. *Precambrian Research*, *212*, 155–168.

[27]. Amponsah, P. O., Kwayisi, D., Awunyo, E. K., Sapah, M. S., Sakyi, P. A., Su, B.-X., Lu, Y., and Nude, P. M (2023b). New evidence for crustal reworking and juvenile arc-magmatism during the Palaeoproterozoic Eburnean events in the Suhum basin, South-East Ghana. *Geological Journal*.

[28]. Block, S., Jessell, M., Aillères, L., Baratoux, L., Bruguier, O., Zeh, A., Bosch, D., Caby, R., and Mensah, E. (2016). Lower crust exhumation during paleoproterozoic (eburnean) orogeny, NW Ghana, West African craton: interplay of coeval contractional deformation and extensional gravitational collapse. *Precambrian Research*, *274*, 82–109.

[29]. Nunoo, S., Hofmann, A., and Kramers, J. (2022). Geology, zircon U–Pb dating and εHf data for the Julie greenstone belt and associated rocks in NW Ghana: Implications for Birimian-to-Tarkwaian correlation and crustal evolution. *Journal of African Earth Sciences*, *186*, 104444.

[30]. Agyei-Duodu, J. (2009). *Geological Map of Ghana 1: 1 000 000*. Geological Survey Department.

[31]. Feng, X., Wang, E., Ganne, J., Amponsah, P., and Martin, R. (2018). Role of volcano-sedimentary basins in the formation of greenstone-granitoid belts in the west african craton: a numerical model. *Minerals*, *8(2)*, 73.

[32]. Feng, X., Wang, E., Amponsah, P. O., Ganne, J., Martin, R., and Jessell, M. W. (2019). Effect of pre-existing faults on the distribution of lower crust exhumation under extension: numerical modelling and implications for NW Ghana. *Geosciences Journal*, *23(6)*, 961–975.

[33]. Sapah, M. S., Agbetsoamedo, J. E., Amponsah, P. O., Dampare, S. B., and Asiedu, D. K. (2021). Neodymium isotope composition of palaeoproterozoic Birimian shales from the Wa-Lawra belt, north-west Ghana: Constraint on provenance. *Geological Journal*, *56(4)*, 2072–2081.

[34]. Baratoux, L., Metelka, V., Naba, S., Jessell, M. W., Grégoire, M., and Ganne, J. (2011). Juvenile Paleoproterozoic crust evolution during the eburnean orogeny (2.2–2.0 ga), western burkina faso. *Precambrian Research*, *191(1-2)*, 18–45.

[35]. Amponsah, P. O., Salvi, S., Béziat, D., Siebenaller, L., Baratoux, L., and Jessell, M. W. (2015). Geology and geochemistry of the shear-hosted julie gold deposit, nw ghana. *Journal of African Earth Sciences*, *112*, 505–523.

[36]. De Kock, G., Armstrong, R., Siegfried, H., and Thomas, E. (2011). Geochronology of the Birim supergroup of the West African craton in the Wa-Bolé region of west-central Ghana: Implications for the stratigraphic framework. *Journal of African Earth Sciences*, *59(1)*, 1–40.

[37]. Amponsah, P. O., Salvi, S., Didier, B., Baratoux, L., Siebenaller, L., Jessell, M., Nude, P. M., and Gyawu, E.A (2016). Multistage gold mineralization in the Wa-Lawra greenstone belt, NW Ghana: The Bepkong deposit. *Journal of African Earth Sciences*, *120*, 220–237.

[38]. Milési, J., Feybesse, J., Pinna, P., Deschamps, Y., Kampunzu, H., Muhongo, S., Lescuyer, J., Le Goff, E., Delor, C., Billa, M. *et al.* (2004). Geological map of africa 1: 10,000,000, sigafrique project. In *20th conference of African geology, BRGM, Orléans, France*, pages 2–7.

[39]. Holden, E.-J., Wong, J. C., Kovesi, P., Wedge, D., Dentith, M., and Bagas, L. (2012). Identifying structural complexity in aeromagnetic data: An image analysis approach to greenfields gold exploration. *Ore Geology Reviews*, *46*, 47–59.

[40]. Forson, E. D., Menyeh, A., and Wemegah, D. D. (2021). Mapping lithological units, structural lineaments and alteration zones in the southern Kibi-Winneba belt of Ghana using integrated geophysical and remote sensing datasets. *Ore Geology Reviews*, *137*, 104271.

[41]. Mohamed, A., Abdelrady, M., Alshehri, F., Mohammed, M. A., and Abdelrady, A. (2022). Detion of mineralization zones using aeromagnetic data. *Applied Sciences*, *12(18),* 9078.

[42]. Yilmaz, I. (2009). Landslide susceptibility mapping using frequency ratio, logistic regression, artificial neural networks and their comparison: a case study from kat landslides (Tokat Turkey). *Computers & Geosciences*, *35(6)*,1125–1138.

[43]. Amponsah, T. Y., Wemegah, D. D., Danuor, S. K., and Forson, E. D. (2023c). Depth-based correlation analysis between density of lineaments in the crystalline basement's weathered zones and groundwater occurrences within the Voltaian basin, Ghana. *Geophysical Prospecting*.

[44]. Bonham-Carter, G. F. (1994). Geographic information systems for geoscientists-modeling with GIS. *Computer methods in the geoscientists*, 13:398.

[45]. Fu, C., Chen, K., Yang, Q., Chen, J., Wang, J., Liu, J., Xiang, Y., Li, Y., and Rajesh, H. (2021). Mapping gold mineral prospectivity based on weights of evidence method in southeast Asmara, Eritrea. *Journal of African Earth Sciences*, 176:104143.

[46]. Ozdemir, A. (2011). GIS-based groundwater spring potential mapping in the sultan mountains (Konya, Turkey) using frequency ratio, weights of evidence and logistic regression methods and their comparison. *Journal of hydrology*, 411*(3-4),* 290–308.

[47]. Van Westen, C. J. (1993). Application of geographic information systems to landslide hazard zonation.

[48]. Chen, Y. and Sui, Y. (2022). Dictionary learning

for integration of evidential layers for mineral prospectivity modeling. *Ore Geology Reviews*, 141:104649.

[49]. Yin, B., Zuo, R., and Xiong, Y. (2022). Mineral prospectivity mapping via gated recurrent unit model. *Natural Resources Research*, *31(4),* 2065–2079.

[50]. Forson, E. D., Amponsah, P. O., Hagan, G. B., and Sapah, M. S. (2023). Frequency ratio-based flood vulnerability modeling over the Greater Accra Region of Ghana. *Modeling Earth Systems and Environment*, *9(2),* 2081–2100.

[51]. Eldosouky, A. M., Abdelkareem, M., and Elkhateeb, S. O. (2017). Integration of remote sensing and aeromagnetic data for mapping structural features and hydrothermal alteration zones in wadi Allaqi area, south eastern desert of Egypt. *Journal of African Earth Sciences*, 130:28–37.

[52]. Elkhateeb, S. O., Eldosouky, A. M., Khalifa, M. O., and Aboalhassan, M. (2021). Probability of mineral occurrence in the southeast of aswan area, egypt, from the analysis of aeromagnetic data. *Arabian Journal of Geosciences*, *14(15),* 1–12.

[53]. Wemegah, D. D., Preko, K., Noye, R. M., Boadi, B., Menyeh, A., Danuor, S. K., Amenyoh, T. *et al*. (2015). Geophysical interpretation of possible gold mineralization zones in kyerano, south-western Ghana using aeromagnetic and radiometric datasets. *Journal of Geoscience and Environment Protection*, *3(04),* 67.

[54]. Forson, E. D. and Amponsah, P. O. (2023). Mineral prospectivity mapping over the Gomoa Area of Ghana's southern Kibi-Winneba belt using support vector machine and naive bayes. Journal of African Earth Sciences, 105024.

[55]. Craw, D. and Campbell, J. (2004). Tectonic and structural setting for active mesothermal gold vein systems, southern alps, new zealand. *Journal of Structural Geology*, *26(6-7)*, 995–1005.

[56]. Blake, F., Grant, K., MacKenzie, D., Scott, J., and Craw, D. (2019). Surficial arsenic redistribution above gold-mineralised zones in east otago, new zealand. *New Zealand Journal of Geology and Geophysics*, *62(4),* 573–587.

[57]. Elkhateeb, S. O. and Abdellatif, M. A. G. (2018). Delineation potential gold mineralization zones in a part of central eastern desert, egypt using airborne magnetic and radiometric data. *NRIAG Journal of Astronomy and Geophysics*, *7(2)*, 361–376.

مدلسازی آینده نگری معدنی بر روی جولی تنمنت از شمال غربی غنا با استفاده از مجموعه داده های ژئوفیزیکی

پرینسه افوری آمپونسا[1] و اریک دومینیک فورسون[2]*

۱ .گروه علوم زمین، دانشکده علوم فیزیکی و ریاضی، دانشگاه غنا، لگون-اکرا، غنا
۲. گروه فیزیک، دانشکده علوم فیزیکی و ریاضی، دانشگاه غنا، لگون-اکرا، غنا

ارسال ۲۰۲۳/۰۹/۲۰، پذیرش ۲۰۲۴/۰۱/۰۳

* نویسنده مسئول مکاتبات: edforson@ug.edu.gh

چکیده:

این مطالعه با استفاده از دو تکنیک آماری فضایی، یعنی مدل‌های ارزش اطلاعات (IV) و وزن شواهد (W of E) مناطق احتمالی وقوع کانی‌سازی طلا را بر روی سکونتگاه جولی در شمال غربی غنا ترسیم کرد. ابتدا، ۱۱۰ مکان، که در آن کانی سازی طلا (Au) مشاهده شده است، با نتایج بررسی میدانی به دست آمده از مجموعه داده‌های سنجش ژئوشیمیایی بسیار غیرعادی شناسایی شدند. از این ۱۱۰ مکان، ۷۷ مکان (نماینده ۷۰ درصد مکان‌های شناخته شده، که طلا در آن مشاهده شده است) به طور تصادفی برای آموزش مدل‌های ذکر شده انتخاب شدند و ۳۳ مکان باقی مانده (مشابه ۳۰ درصد از وقوع شناخته شده طلا) برای اعتبار سنجی استفاده شدند. ثانیاً، یازده فاکتور شرطی سازی معدنی (لایه‌های شواهد) شامل سیگنال تحلیلی، کاهش به استوا (RTE)، چگالی خطی (LD)، چگالی پورفیری، غلظت پتاسیم، غلظت توریم، غلظت اورانیوم، نسبت پتاسیم به توریم، نسبت اورانیوم به توریم لایه‌های غلظت، زمین‌شناسی و آرسنیک از مجموعه داده‌های ژئوفیزیکی، زمین‌شناسی و ژئوشیمیایی به دست آمدند. متعاقباً، با سنتز این یازده لایه شواهد با استفاده از دو تکنیک آماری فضایی، دو مدل آینده نگری معدنی در یک محیط سیستم اطلاعات جغرافیایی (GIS) ایجاد شد. در نهایت، مدل‌های آینده‌نگری معدنی تولید شده با استفاده از ناحیه زیر منحنی ویژگی‌های عملیاتی گیرنده (AUC) اعتبارسنجی شدند. نتایج به‌دست‌آمده نشان داد که مدل IV تولید شده دارای دقت پیش‌بینی بالاتری در مقایسه با مدل پیش‌بینی مواد معدنی تولید شده توسط W of E با امتیاز AUC آن‌ها به ترتیب ۰/۷۵۱ و ۰/۷۴۳ است.

کلمات کلیدی: مدلسازی آینده نگری معدنی، ارزش اطلاعات، وزن شواهد، داده‌های هوا مغناطیسی، داده‌های رادیومتری هوابرد.